



Analyzing Low Frequency Seismic Events at Cerberus Fossae as Long Period Volcanic Quakes

Sharon Kedar, Mark P Panning, Suzanne E Smrekar, Simon C Stähler, Scott D King, Matthew P Golombek, Michael Manga, Bruce R Julian, Brian Shiro, Clement Perrin, et al.

► To cite this version:

Sharon Kedar, Mark P Panning, Suzanne E Smrekar, Simon C Stähler, Scott D King, et al.. Analyzing Low Frequency Seismic Events at Cerberus Fossae as Long Period Volcanic Quakes. *Journal of Geophysical Research. Planets*, 2021, 126 (4), pp.e2020JE006518. 10.1029/2020je006518 . hal-03519089

HAL Id: hal-03519089

<https://hal.science/hal-03519089>

Submitted on 10 Jan 2022

HAL is a multi-disciplinary open access archive for the deposit and dissemination of scientific research documents, whether they are published or not. The documents may come from teaching and research institutions in France or abroad, or from public or private research centers.

L'archive ouverte pluridisciplinaire **HAL**, est destinée au dépôt et à la diffusion de documents scientifiques de niveau recherche, publiés ou non, émanant des établissements d'enseignement et de recherche français ou étrangers, des laboratoires publics ou privés.

Special Section:

InSight at Mars

Key Points:

- Low Frequency (LF) events that share attributes of volcanic quakes are traced to a young volcanic region on Mars
- LF events are modeled as deep volcanic quakes caused by pressure-driven flow across a channel at Cerberus Fossae
- LF attributes are matched by fluids less viscous and of higher fluxes than terrestrial flood basalts

Supporting Information:

Supporting Information may be found in the online version of this article.

Correspondence to:

S. Kedar,
Sharon.Kedar@jpl.nasa.gov

Citation:

Kedar, S., Panning, M. P., Smrekar, S. E., Stähler, S. C., King, S. D., Golombek, M. P., et al. (2021). Analyzing low frequency seismic events at Cerberus Fossae as long period volcanic quakes. *Journal of Geophysical Research: Planets*, 126, e2020JE006518. <https://doi.org/10.1029/2020JE006518>

Received 8 MAY 2020

Accepted 15 FEB 2021

Author Contributions:

Conceptualization: Sharon Kedar, Mark P. Panning, Suzanne E. Smrekar, Scott D. King, Matthew P. Golombek, Bruce R. Julian, Domenico Giardini, William B. Banerdt

Formal analysis: Sharon Kedar, Mark P. Panning, Simon C. Stähler, Bruce R. Julian

Investigation: Sharon Kedar, Scott D. King, Michael Manga, Bruce R. Julian, John A. Power

















Methodology: Sharon Kedar, Suzanne E. Smrekar, Domenico Giardini

Resources: Brian Shiro

Software: Mark P. Panning

Supervision: Sharon Kedar

Analyzing Low Frequency Seismic Events at Cerberus Fossae as Long Period Volcanic Quakes

Sharon Kedar¹ , Mark P. Panning¹ , Suzanne E. Smrekar¹ , Simon C. Stähler² , Scott D. King³ , Matthew P. Golombek¹ , Michael Manga⁴ , Bruce R. Julian⁵ , Brian Shiro⁶ , Clement Perrin⁷ , John A. Power⁸ , Chloe Michaut⁹ , Savas Ceylan² , Domenico Giardini² , Philippe H. Lognonné⁷ , and William B. Banerdt¹ 
¹Jet Propulsion Laboratory, California Institute of Technology, Pasadena, CA, USA, ²Institute of Geophysics, Department of Earth Sciences, ETH Zurich, Zurich, Switzerland, ³Virginia Tech, Blacksburg, VA, USA, ⁴University of California, Berkeley, CA, USA, ⁵Department of Earth Sciences, Durham University, Durham, UK, ⁶USGS, Hawaiian Volcano Observatory, Hilo, HI, USA, ⁷Université de Paris, Institut de physique du globe de Paris, CNRS, Paris, France, ⁸USGS, Alaska Volcano Observatory, Fairbanks, AK, USA, ⁹ENS de Lyon, Lyon, France

Abstract The InSight Mission began acquiring the first seismic data on Mars in early 2019 and has detected hundreds of events. The largest events recorded to date originate at Cerberus Fossae, a young volcanic region characterized by high volume, low viscosity lava flows. A handful of Low Frequency (LF) quakes that share key attributes of Long Period quakes recorded on Earth's volcanoes are also traced to Cerberus Fossae. This study explores whether a traditional volcanic source model that simulates the generation of tremor as pressurized fluid makes its way through a channel at depth, can explain these atypical LF events. We consider a wide range of physical parameters including fluid viscosity, the ratio of driving pressure to lithostatic pressure, aspect ratio of the channel, and the equilibrium channel opening. We find that the model can produce the observed seismic signature, with a combination of low-viscosity magma and high volume flux of $\sim 10^4 - 10^5 \text{ m}^3/\text{s}$ that are within an order-of-magnitude agreement with Cerberus Fossae lava flow properties deduced from analysis of lava flow dimensions. It is impossible, however, at this stage to conclude whether or not this is a likely explanation for Mars, as the model results in fluxes that are extreme for Earth yet are just within bounds of what has been inferred for Cerberus Fossae. We therefore conclude that we cannot rule out active magma flow as the mechanism responsible for the atypical LF events that likely originate from Cerberus Fossae.

Plain Language Summary A number of Marsquakes are located at a region of Mars that hosted geologically recent volcanic eruptions. A subset of these events resemble seismic events recorded at volcanoes on Earth. We set out to study whether these events can be explained by fluid flow at depth, using a model of fluid flow through a channel. We find that low viscosities and high flow rates that are within an order-of-magnitude agreement with flow properties deduced from modeling of Cerberus Fossae lava flows are required to match the observed events in question. It is impossible at this stage of the InSight mission, however, to conclude whether or not this is a likely explanation for Mars.

1. Introduction

The Interior Exploration using Seismic Investigations, Geodesy and Heat Transport (InSight) mission, which landed on November 26, 2018, placed the first ultra-sensitive Very Broad Band Seismometer on the Martian surface (Banerdt et al., 2020). Not unexpectedly, the sensitivity of the seismometer (Lognonné et al., 2019) on a predictably quiet planet with a thin atmosphere has enabled the deciphering of its seismic signatures, much of which is still under investigation (Lognonné et al., 2020). Since the completion of the seismic installation 72 sols after landing, a few distinct event types that appear to originate in the planet's interior have been identified (Giardini et al., 2020): Low Frequency (LF) events with energy below 1 Hz, Broadband (BB) events that span frequencies below and above 1 Hz, High Frequency (HF) events with frequency content predominantly above 1 Hz, and events that are confined to a narrow 2.4 Hz resonance atop a background “hum” that is dominated by this frequency. The Martian crust appears to induce a significant degree of scatter into waves propagating through it, which makes it difficult in most cases to identify clear P and S wave arrivals. Moreover, no events with readily identifiable surface waves have been observed to date.

Visualization: Sharon Kedar, Mark P. Panning, Simon C. Stahler, Simon C. Stahler
Writing – original draft: Sharon Kedar, Mark P. Panning, Suzanne E. Smrekar, Scott D. King, Matthew P. Golombek, Michael Manga, Bruce R. Julian
Writing – review & editing: Sharon Kedar, Mark P. Panning, Suzanne E. Smrekar, Simon C. Stähler, Scott D. King, Matthew P. Golombek, Michael Manga, Bruce R. Julian, Brian Shiro, Clement Perrin, John A. Power, Chloe Michaut, Savas Ceylan, Domenico Giardini, Philippe H. Lognonné, William B. Banerdt

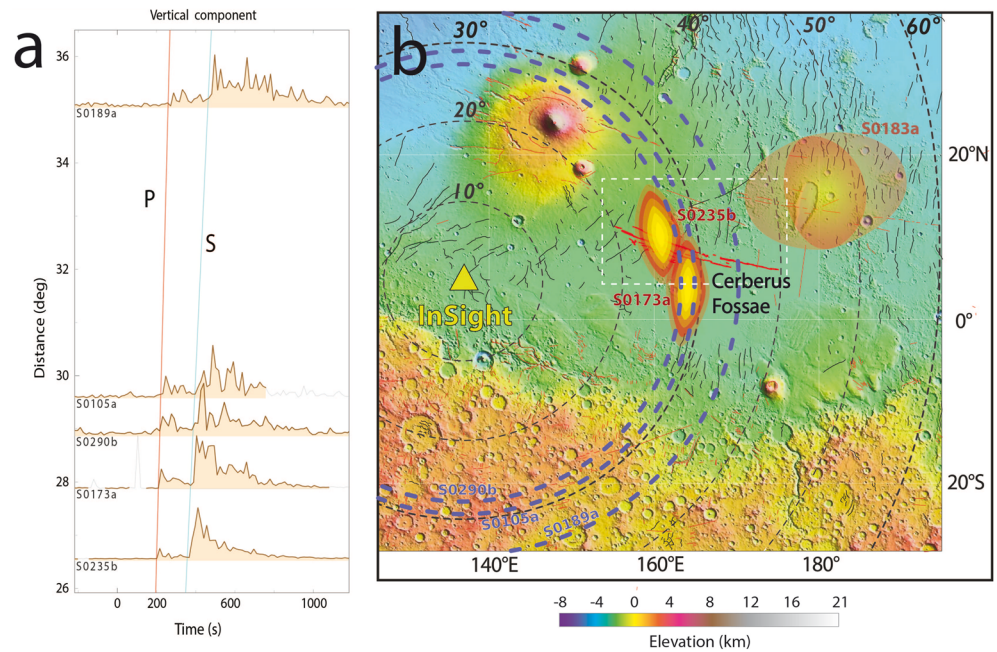


Figure 1. (a) Spectral envelopes for five of the low frequency family events, aligned with the direct P- and S-wave travel times using a reference model. Following Giardini et al. (2020), the envelopes are computed by summing the spectral amplitudes over a frequency band tailored for each event depending on their spectral content. The spectrograms are calculated using window lengths of 30 s with an overlap of 50% on acceleration data after instrument correction. The event names are shown on the left hand side of the corresponding envelopes. See (InSight Marsquake Service, 2020) for detailed information on the seismic events and InSight seismicity catalog. (b) Mars Orbiter Laser Altimeter topographic map of Elysium Planitia from Giardini et al. (2020), showing the location of the InSight lander (yellow triangle), the location of the two largest events recorded to date: S0173a and S0235b and the estimated epicentral distances (purple circles) of S0105a, S0189a, and S0290b. Red to yellow ellipsoids are the estimated locations of events S0173a and S0235b, both identified by Giardini et al. (2020) as Low Frequency (LF) events; The epicenter location estimate of an additional event well outside Cerberus Fossae, S0183a, is displayed with two shaded ellipses, representing distance uncertainties of 5° and 10°. The marked rectangular area is elaborated upon in Section 2.1 and Figure 3. LF, Low Frequency.

The two largest events recorded on Mars to date (S0173a and S0235b, [Giardini et al., 2020]) present a dominant S-phase and clear P-arrivals, and an unambiguous P- and S-phase polarization that in conjunction with the epicentral distance are located in the general area of Cerberus Fossae (Figure 1 and Giardini et al., 2020). Cerberus Fossae is a young geologic area ~1,500 km east of the InSight landing site at Elysium Planitia, characterized by fissures and faults that cut across what are estimated to be among the youngest (2.5–10 m.y.) lava flows on the surface of Mars (Vaucher et al., 2009) and hosted explosive eruptions 50–200 ka (Horvath et al., 2020). The geological history of Cerberus Fossae is discussed in detail in Section 2.1. S0173a and S0235b are the quakes with highest signal-to-noise ratio and have all the characteristics of tectonic events as their frequency content and decay are consistent with a tectonic origin and with a Brune stress-drop formulation (Giardini et al., 2020).

1.1. LF Events at Cerberus Fossae, and the Possibility of Their Volcanic Origin

About 10% of the several hundreds of events identified to date are characterized by a 10–20 min duration and frequencies lower than 1 Hz and are termed “LF” by Giardini et al. (2020). Three LF events (S0105a, S0189a, and S0290b) have P and S arrivals that place their epicentral distance in Cerberus Fossae (Figure 1). However, unlike S0173a and S0235b, their P and S arrivals are less pronounced, their S/P amplitude ratio is lower, and, as can be seen in the time-spectra plot in Figure 2 they display persistent spectral peaks and arguably a poorer fit to an attenuated Brune source formulation. This could be partly attributed to their smaller magnitude and low signal-to-noise-ratio, yet their spectral characteristics are intriguing in that they appear to have spectral peaks that are stable throughout the duration of the quake whereas a lower

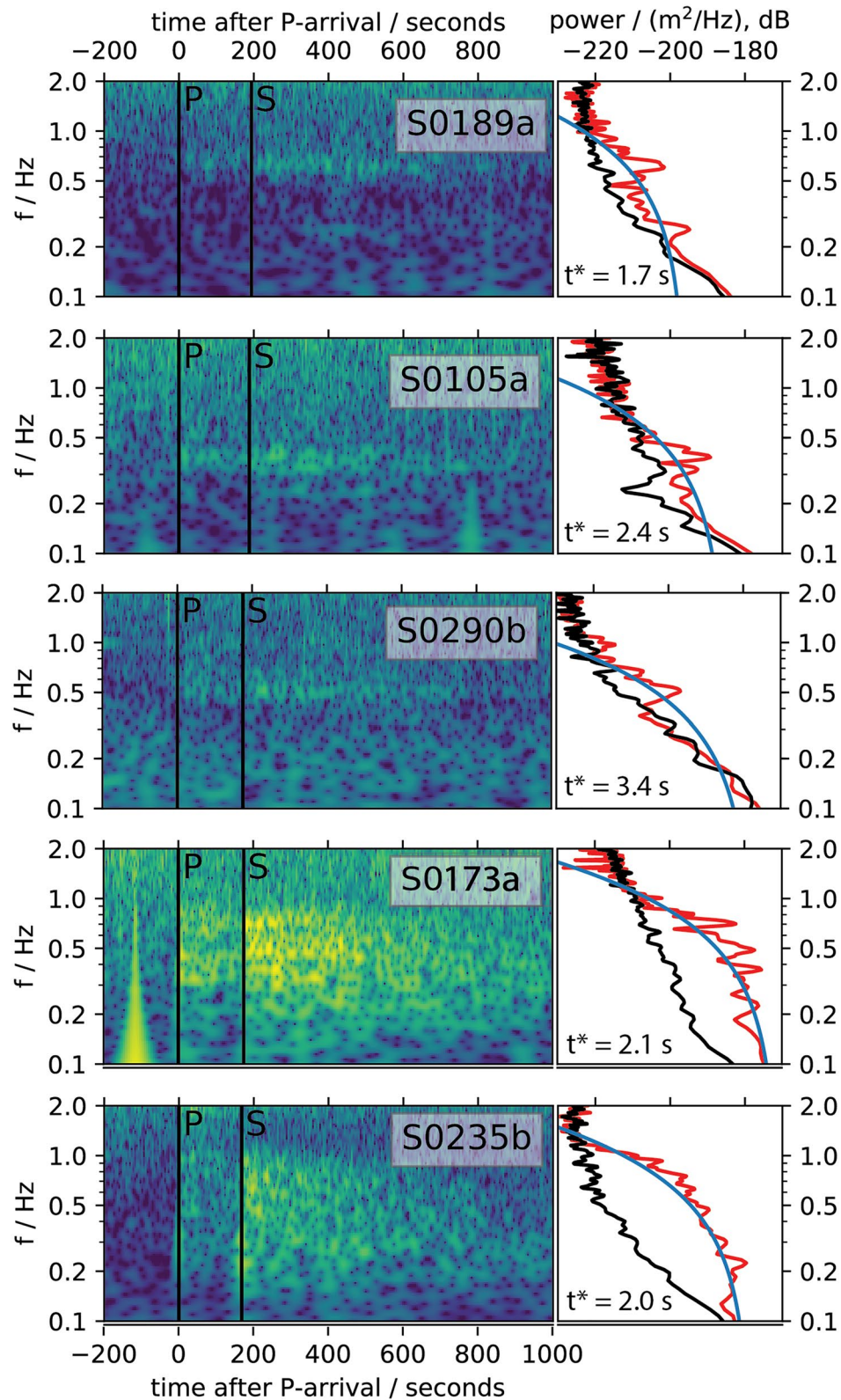


Figure 2. Left: Time-Spectra plot of S0105a, S0173a, S0189a, S0235b, and S0290b. Right: A fit to a Brune source formulation (Brune, 1970) with presumed stress drop of 1 MPa and a corner frequency of 1 Hz, affected by attenuation as described by the t^* provided in each sub-figure (Red line: Event spectrum; Black line: Pre-event noise spectrum; Blue line: Event data fit to an attenuated Brune source model) The smaller events' frequency signature is narrower than the larger S0173a and S0235b, and their fit to a Brune source model is poorer.

magnitude tectonic quake would typically result in a more uniform amplitude reduction across the entire frequency spectrum. Moreover, S0189a and S0105a in particular are dominated by two distinctly different frequencies (~ 0.6 Hz and ~ 0.35 Hz, respectively), which makes it hard to reconcile with a pure propagation effect if the two events originate from the same general location.

On Earth, events that are characterized by emergent arrivals, low S/P ratios, and by a dominant frequency are frequently found in volcanic regions. Such events, termed “Long Period (LP) quakes” originate by fluid flow (magma, water, gas, and their combination) within Earth’s magmatic and hydrothermal systems, and their properties are largely attributed to their source rather than propagation effects (see review of volcanic seismicity in Section 2.2). Naturally, such attributes are not unique to volcanic LP quakes. For example, Martire et al. (2020), intrigued by the “monotonic” nature of S0189a, interpreted it as an atmospheric waveguide effect. Here we pursue an alternative explanation to Martire et al. (2020). The young age of both the volcanic flows and even younger fault scarps at Cerberus Fossae, and its seismicity evidenced by S0173a and S0235b pose the possibility of a remnant, subsurface magma body or thermal anomaly at depth capable of producing seismic activity (see Section 2.1). In the discussion that follows we test this possibility by investigating whether the characteristics of S0105a and of S0189a can be modeled by a classical LP Quake volcanic source model (Julian, 1994). This model, which is described in detail in Section 2.3, is used to match the predominant spectral peaks of S0105a (~ 0.35 Hz) and S0189a (~ 0.6 Hz), their duration (~ 15 min), and their observed amplitudes. Subsequently, we use the modeled source properties (fluid viscosity, flux, and source geometry and elastic properties) to test whether a volcanic source beneath Cerberus Fossae is plausible.

1.2. Assumptions and Methodology

1.2.1. Location of “LF” Events at Cerberus Fossae

Since the locations of S0105a, S0189a, and S0290b are not uniquely defined beyond an epicentral distance, one possibility is that they do not originate within Cerberus Fossae, or are perhaps atmospheric in origin as postulated by Martire et al. (2020). In this case their signature could be attributed to a propagation effect such as a crustal wave guide. In that case the propagation effect would have to differ between the events to account for the different spectral peaks. If this were the case we might also expect to see similarly persistent spectral peaks in many LF events, which is generally not the case (See Giardini et al., 2020, Figure 4). Since the two largest events recorded to date (S0173a and S0235b) unambiguously originate at a plausibly active geological region, for the purpose of this study, we are going to assume that LF events with similar epicentral distance originate from the same region, in which case their different spectral characteristics may be attributed at least in part to a different source process.

1.2.2. Source Depth and Propagation Effects

Implicit in presuming a predominantly source effect is the implication that propagation and shallow crust scattering effects, which are arguably prominent on Mars (Giardini et al., 2020), are minimal. This can only be the case if the source is sufficiently deep, and we therefore make the further assumption that the source is deeper than 60 km, that is, well below the Martian Moho, consistent with the fact that to date there has been no orbital evidence of active surface volcanism on Mars. The wave propagation models used to model the observed amplitude are discussed in Section 2.5.1.

1.2.3. Possible Source Models

Volcanic and fluid flow sources with similar seismic signatures to S0105a and S0189a have been studied in great detail for a vast range of source mechanisms, over broad physical, fluid dynamical, and geothermal regimes in various geological settings. There exists a broad array of physical models that are capable of successfully reproducing the main characteristics of flow-induced oscillatory phenomenon (Chouet, 1996), and we provide a brief review of these in Section 2.2. For the purpose of this study, we adopt the generic model of Julian (1994), which is based on a nonlinear excitation of oscillations by fluid flow, analogous to the excitation of musical wind instruments (Section 2.3). This model has been successfully used to explain many characteristics of terrestrial tremor that can be explained as the superposition of many LP events, and encompasses a range of physical properties of the fluid, solid, and the forces that drive it. The model treats the source as a buried channel or valve through which fluid, driven by a pressure gradient along the channel,

flows. Under certain conditions channel wall oscillations are induced, and the model yields the amplitude and channel wall velocity as a function of time, as well as the velocity of the fluid. The wall oscillations are then fed through a seismic wave propagation model that predicts the body-wave signal amplitudes at a presumed distance from the source.

1.2.4. Bayesian Exploration of the Source Parameter Space

Key input parameters are the source depth and its physical dimensions, elastic and inelastic properties of the solid, fluid viscosity and density, and the driving pressure gradient. While the parameter space can be a-priori narrowed down using geological and geodynamical considerations (Section 2.4), the study of the remainder space is still a daunting task. We therefore choose to proceed with a Bayesian approach (Section 2.5), in which each model trial is either rejected based on the observed constraints or informs the next trial, changing one parameter at a time, and marching toward a solution that is more probable. This statistical approach to the problem is an efficient way to identify the possible physical regimes that may be consistent with the observed properties of S0105a and S0189a. Once the allowable parameter space under the assumptions delineated above is determined, we explore whether or not the source properties (viscosity, flux, channel properties) are consistent with our inferred knowledge of past activity on Mars and with fluid induced seismicity on Earth, and whether or not the modeled source is geologically and geodynamically plausible.

1.2.5. Scope of the Investigation

Finally, before proceeding with a detailed discussion of the analysis, it is important to emphasize that given the lack of active surface volcanism and the still limited seismic data, an investigation of implied subsurface fluid flow induced seismicity on Mars is speculative. Furthermore, the characteristics of the observed seismic signals coupled with the breadth of fluid source models and physical parameters that can explain them makes the problem inherently under-constrained. Our knowledge of the Martian interior, while far better constrained since the InSight mission inception, is still ambiguous. Consequently, at this stage of the mission, S0105a and S0189a can be explained by any number of source and propagation models. With these considerations in mind this study should be treated as a thought experiment. We investigate one possibility out of many: whether or not a subset of seismic events (S0105a and S0189a) could be generated by fluid flow through a conduit located at depth within Cerberus Fossae, and if so, what is the physical parameter space (source depth, magma viscosity, and flux) and are parameters consistent with our understanding of volcanic activity at Cerberus Fossae.

2. Exploring Mars Tremor as Seismic Signals as Induced by Fluid Motion

2.1. Geologic Setting and Evidence for Relatively Recent Volcanic and Fluvial Activity at Cerberus Fossae

Mars has abundant evidence for volcanism and liquid water outflows on its surface. However, most are billions of years old. In contrast, Cerberus Fossae is among the youngest tectonic structures on Mars that is the source for large expulsions of water and lava. It is a ~1,250 km long series of fossae that are about 1,500 km to the east of the InSight lander (Figures 1 and 3). The fossae are the freshest fractures on Mars with over 500 m of vertical throw, little sediment infill (Vetterlein & Roberts, 2009) and fresh boulder trails (from boulder falls) attributed to recent paleomarsquakes (Brown & Roberts, 2019; Roberts et al., 2012). Three outflow channels were carved by catastrophic floods that emanated from the structures (Burr, Grier, et al., 2002; Burr, McEwen, et al., 2002). Athabasca Valles extends 1,200 km to the west, Marte Valles extends 1,800 km to the east and then northeast, and Grjota Valles extends to the northeast.

Volcanism in central Elysium Planitia was active over the last 250 Ma and covered the Cerberus Plains, south-east of Cerberus Fossae (Vaucher et al., 2009) and coated the outflow channels (Jaeger et al., 2007, 2010). The youngest volcanic flow (~2.5 Ma) extended to the western lava basin (Vaucher et al., 2009), only 1,500 km east of the InSight lander (Golombek et al., 2017, 2020). The close association between large volumes of water and lava emanating from the same structure has led to interpretations that the grabens are underlain by dikes that may have interacted with ice (Cassanelli & Head, 2018; Head et al., 2003; Nahm et al., 2016), possibly via release of pressurized groundwater confined below a cryosphere (e.g., Cassanelli & Head, 2018; Marra et al., 2014, and references therein). Cerberus Fossae fault offset occurred after the most recent flow

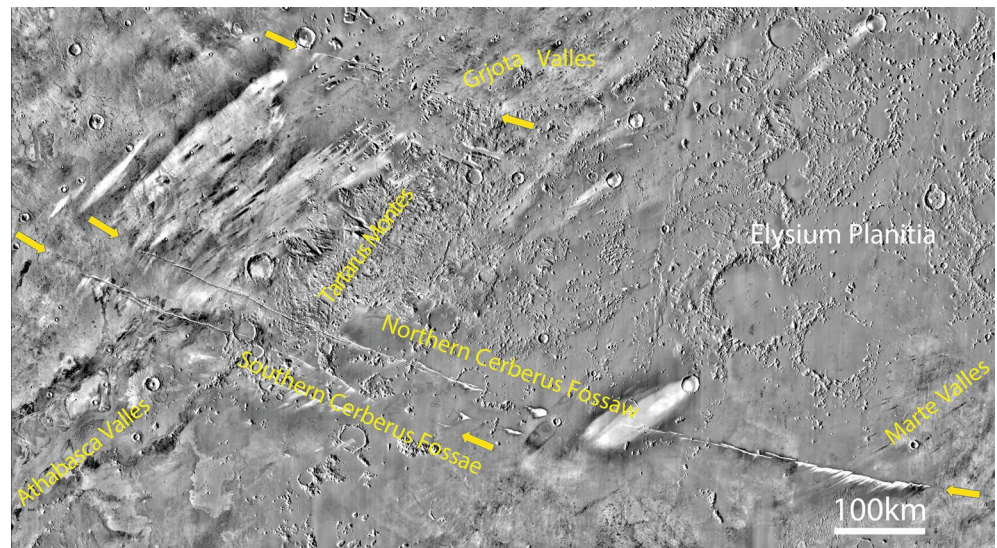


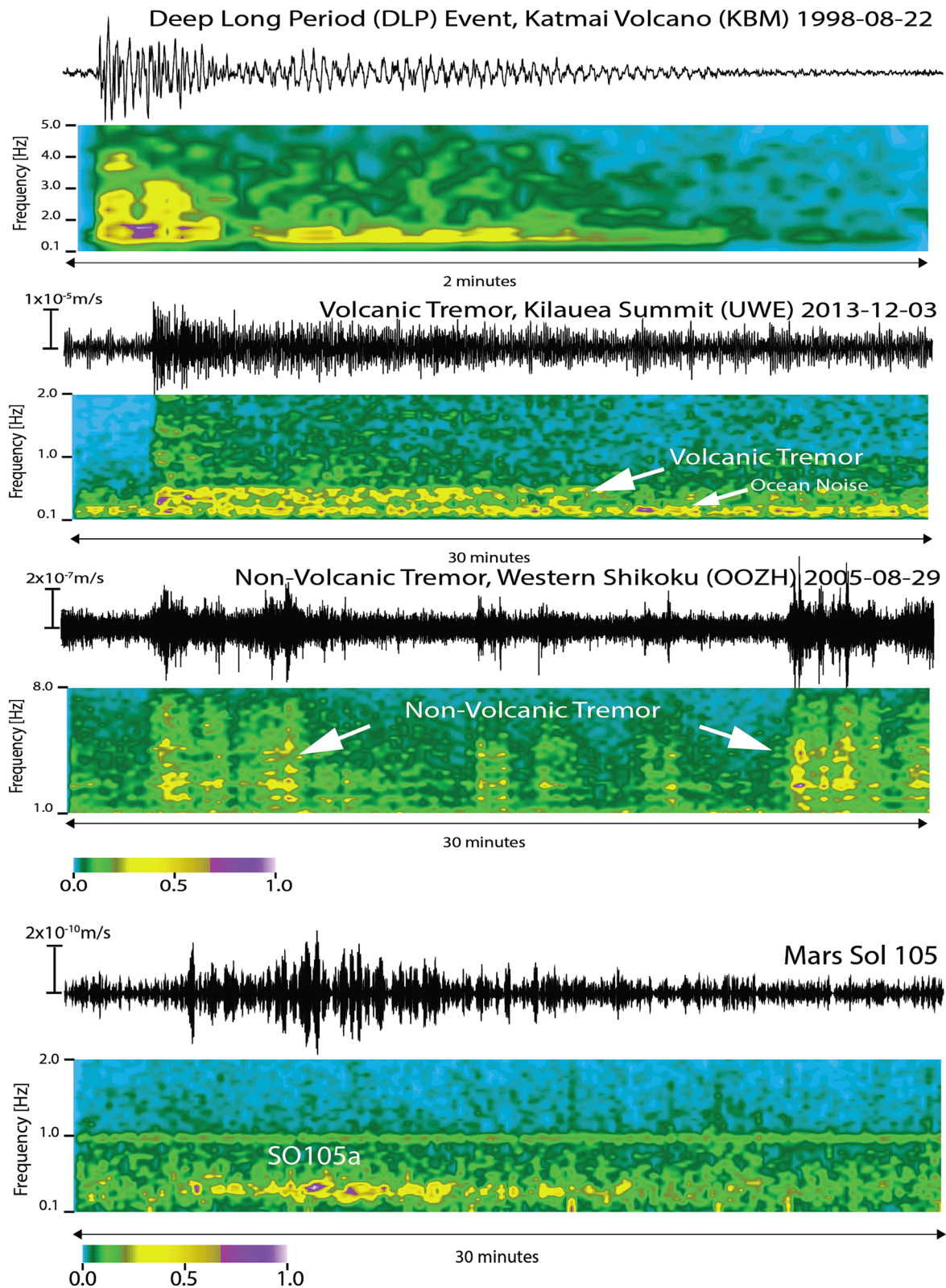
Figure 3. Thermal Emission I maging System (THEMIS) daytime thermal infrared mosaic of Cerberus Fossae and Elysium Planitia (Area depicted by a rectangular box in Figure 1). Young fractures associated with northern and southern Cerberus Fossae and fracture system near Grjota Valles are denoted by orange arrows at their ends. Southern Cerberus Fossae is the source for catastrophic outbursts of water that carved Athabasca Valles and later filled the channel with basaltic lava flows (note channels and streamlined forms). Grjota Valles and Marte Valles were similarly sourced from the adjacent fracture systems shown. THEMIS daytime infrared images (100 m/pixel) include thermal properties of surface materials. Bright streaks extending to the southwest behind craters and fractures are composed of fine-grained material with low thermal inertia (likely dust). Dark flows adjacent to southern Cerberus Fossae have high thermal inertia. Thermal inertia is a material's resistance to a change in temperature. THEMIS, Thermal Emission I maging System.

(Vetterlein & Roberts, 2009) and is predicted to be active today (Taylor et al., 2013). Several seismic events detected by InSight appear to have originated from Cerberus Fossae (Figure 1 and Giardini et al., 2020). Athabasca Valles is unusual in that it is interpreted to have been initially carved by water and subsequently coated by a single, thin volcanic flow. The presence of features such as teardrop shape islands and giant ripples, similar to those seen in Channeled Scabland, are interpreted to indicate erosion via catastrophic (large, short) floods (Burr, Grier, et al., 2002; Tanaka, 1986). Lava flow morphology, including a platy crust, defines the boundaries of an apparently single volcanic flow that poured into preexisting fluvially incised channel.

There is abundant evidence for water ice in the polar caps and in the shallow subsurface down to the mid-latitudes (Feldman et al., 2008). Furthermore, there is evidence for significant shallow ice deposits at lower latitudes (Bramson et al., 2015) likely left from expected large excursions of the pole of rotation. In addition, rover and orbital missions have provided clear evidence for extensive surface and subsurface water in the past (Ehlmann et al., 2011; Grotzinger et al., 2015; Squyres et al., 2006) including the possibility of ancient oceans (Clifford & Parker, 2001). Current surface pressure and temperature conditions are outside the stability of liquid water or ice near the equator. However, increased pressure and temperature with depth near the equator indicates liquid water could be stable at a few km depth (Clifford & Parker, 2001). The morphologic evidence for catastrophic floods emanating from Cerberus Fossae at multiple locations clearly indicates that some processes liberated vast volumes of water from depth within the past few Ma (Burr, Grier, et al., 2002).

2.2. A Brief Summary of LP Volcanic Seismicity Observations and Models

The examples of terrestrial volcanic and non-volcanic tremor are numerous. A comprehensive review of the types of events observed on Earth's volcanoes and the physical processes that might generate them can be found in Chouet and Matoza (2013) and McNutt (2005) among others. In exploring the analogies to terrestrial tremor, we limit our discussion to the examination of LF (<1 Hz) continuous, quasi monochromatic events.



2.2.1. Characteristics of LP Volcanic Seismicity

Figure 4 shows a handful of representative examples of volcanic and non-volcanic tremor recorded on Earth.

Quasi monochromatic LP tremor is found both deep below volcanic regions and at more shallow depths during the buildup to eruptions. Perhaps one of the most notable examples of deep tremor is described by Aki and Koyanagi (1981) who observed continuous tremor episodes (>40 km) underneath Kilauea volcano. They attributed the seismicity to a steady magma transport process that is confined to the subsurface. Since Aki and Koyanagi (1981) many similar episodes of deep Hawaiian tremor have been observed (Wech & Thelen, 2015). The frequencies of deep Hawaiian tremor are on average higher than those shown in Figure 2, but their duration is similar. Pitt and Hill (1994) identified swarms of LP quakes 10–28 km underneath Mammoth Mountain with a dominant spectral peak ~ 1.5 Hz. Although individual events last about a minute there are many recorded instances in which such LP events merge into a background monochromatic hum. LP events were recorded at ~ 30 km depths at Pinatubo in early June 1991 (Harlow et al., 1996), and were attributed to a basaltic intrusion during the build-up phase which led to the eruption later that month. Deep Long Period (DLP) (10 – 45 km) tremor was reported over a period of several years in the Aleutian Arc by the Alaska Volcano Observatory by Power et al. (2004). Aleutian DLP events were both solitary and at times clustered over a period of 1–30 days (Power et al., 2004). Non-volcanic tremor, observed during episodic slip events at subduction zones (Rogers & Dragert, 2003) and other tectonic settings (Tao et al., 2020), shares some of the same characteristics, though it mostly appears as low amplitude, higher-frequency continuous vibrations that accompany episodes of concurrent slow slip along the plate boundary.

A notable example of non-volcanic tremor associated with aseismic slip was described by Shelly et al. (2007) who identified swarms of LF (~ 1 –5 Hz) quakes that occur as shear faulting on the subduction zone interface. An example of that episode is shown in Figure 4. While non-volcanic tremor is a possibility that likely involves the increase of pore fluid pressure (Thomas et al., 2009), the characteristics of S0105a and S0189a more closely resemble numerous examples of volcanic events both in their typically lower frequency content and in their more monochromatic signature. For that reason, we leave the discussion of non-volcanic tremor modeling of Mars events to future studies and focus here on the possibility that Cerberus Fossae LF events might be induced directly by fluid flow as occurs on Earth's volcanoes.

Volcanic LP events are characterized by a brief onset, a long (minutes to hours) coda, and quasi monochromatic signature (Chouet & Matoza, 2013). LP Events that precede eruptions and explosive activity are typically several kilometers deep, and are easier to detect than DLP events. In many instances, individual LP events merge into background tremor as activity intensifies and eruption nears. Classic examples of such activity are the tremor that preceded the 1980 Mount St. Helens eruption (Fehler, 1983) and the awakening of Redoubt volcano in 1989 after a 23-year quiescence (Chouet et al., 1994). Many similar examples are cited in Chouet and Matoza (2013) and McNutt (2005).

It is important to note that tremor recorded on Earth's volcanoes is sufficiently strong to be recorded on local networks (Figure 4), yet rarely, if ever, are such events recorded teleseismically thousands of kilometers away. The absence of ocean noise on Mars and the quiet atmospheric conditions in the night mean that signals ~ 100 times smaller amplitude can be recorded there compared to Earth. By comparison, if any of the events shown in Figure 2 occurred on Earth they would be obscured by the background noise. Therefore, in examining whether or not Low-Frequency Martian events could be volcanic in nature, establishing the resemblance to terrestrial analogs is only a first step. In order to fully answer whether or not these seismic events are volcanic a physical model that endeavors to match the observed event duration, frequency signature and amplitude has to be constructed, and is the main focus of this investigation.

Figure 4. Examples of notable volcanic and non-volcanic tremor and low-frequency events. Top: A 33.6 km deep LP event recorded ~ 30 km away from Katmai volcano (Power et al., 2004) shows the characteristics low frequency of fluid-flow-induced seismic signals. Second Row: A ~ 20 -min long tremor recorded locally at Kilauea Volcano, Hawai'i. Third row: A non-volcanic tremor episode in Northwestern Shikoku described by Shelly et al. (2007). Bottom: S0105a velocity record shown for reference. Note that that S0105a is at a much greater distance and much smaller amplitude from the source compared to the terrestrial examples, and would not be observable on Earth.

2.2.2. Volcanic Tremor Models

There are several features of volcanic tremor that provide insights into the mechanisms that generate the signals. As described above, the signals are long (tens of minutes), dominated by LP energy compared to tectonic quakes (peak around 0.5 Hz), the dominant frequency does not change systematically over time, and the source must be strong enough to produce signals recorded >100 km away. Fluid flows are subject to many kinds of instabilities, which might conceivably excite seismic waves and cause volcanic tremor. There are a host of processes that can produce long-period tremor-like signals, either from the source or by exciting resonances of structures around the source. We provide here a brief summary of some of the volcanic tremor source models that are discussed in the literature.

Magmatic and hydrothermal systems commonly generate LP events and tremor that have periods similar to those recorded on Mars, typically 0.2–2 s (Chouet, 1996). LP events have durations similar to earthquakes, whereas tremor can last for minutes to days. The frequency contents are similar, however, suggesting a common source process. Most interpretations of LP tremor signals appeal to exciting crack resonance by moving fluids: magma, aqueous fluids, or gas. Very Long Period (VLP) signals, 0.01–0.5 Hz, are usually attributed to variations in the inertia of magma and gases flowing through conduits (Chouet & Dawson, 2016; Chouet & Matoza, 2013; Ohminato et al., 1998). LP and VLP events and tremor are now routinely documented at volcanoes, before, during and after eruptions. Inversions of those signals have been used to constrain the geometry of dikes (Chouet & Dawson, 2011; Lyons & Waite, 2011), sills (Dawson et al., 2011), conduits (Liang et al., 2020), and the properties of the magma within those bodies (Kumagai & Chouet, 1999).

Quantitative interpretations of LP events and tremor generally build on a model for the resonance of a fluid-driven crack, originally developed by Aki et al. (1977) with many further modifications. Chouet and Matoza (2013) provide a comprehensive review of the many possible origins of tremor sources: magma-water interactions, magma degassing, magma fragmentation, multiple stick-slip events, or self-sustained fluid oscillations. Episodic release of pressurized fluids from hydrothermal systems can produce tremor (Kawakatsu et al., 2000; Kumagai et al., 2005). Non-volcanic tremor seen in deep fault zones may have a similar origin (Thomas et al., 2009). In basaltic systems, unsteady transport of melt and gas can produce LP signals (Ohminato et al., 1998). Vulcanian eruptions can also produce LP events through feedback between fracturing and gas escape (Neuberg et al., 2006). Tremor at volcanoes (Hotovec et al., 2013; Lesage et al., 2006) and geysers (Karlstrom et al., 2013) sometimes show gliding signals (systematically evolving dominant frequencies) that imply that properties and geometries can change over the timescale that signals are generated (McNutt, 2005).

In addition to waves produced by exciting transport pathways, other processes can produce tremor-like signals. Slow crack propagation in unconsolidated or damaged rock can produce sustained LP signals (Bean et al., 2014; Namiki et al., 2018). Geysers also produce harmonic tremor within the fluid itself, from the ascent of bubbles (Munoz-Saez et al., 2015) or the collapse of bubbles (Kedar et al., 1998; Vandemeulebrouck et al., 2013). These signals are too weak, however, to be recorded more than tens to hundreds of meters from geysers (Ardid et al., 2019; Wu et al., 2019).

Here we assume that the tremor is generated by fluid transport within a subsurface pathway. We do not favor processes involving magma fragmentation as we see no evidence of surface eruptions. Nor do we consider geyser-like processes since we consider only deep sources for the reasons described in Section 1.2. Because the fluids being transported are not shallow (no evidence for surface eruptions of fluids), we assume that there are no bubbles in the fluid and hence the fluid can be treated as incompressible. The long duration of the signal suggests sustained flow, not an impulsive event. We thus apply the generic model developed by Julian (1994), which considers the flow of an incompressible fluid through a channel with compliant, elastic walls that produces self-excited oscillations. As discussed in Section 2.5, we use a Bayesian approach to explore the broad physical parameter space that the Julian (1994) model presents to answer the following questions: can LF seismic events at Cerberus Fossae be explained by fluid flow at depth? If so, what are the flow properties and physical regimes that best match the observations and are they consistent with our current knowledge of the thermal state of the planet.

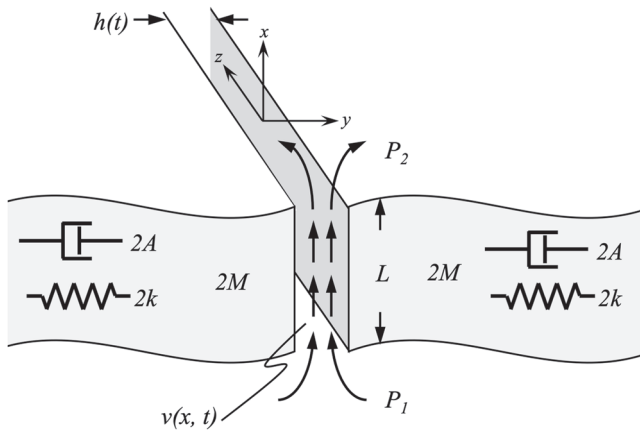


Figure 5. Lumped-parameter model of the generation of volcanic tremor. Viscous, incompressible fluid flows from upstream (bottom) to downstream (top) reservoir through a channel of length L with imperfectly elastic walls, modeled as movable but rigid blocks of mass $2M$, spring stiffness $2k$, and damping constant $2A$ (all measured per unit distance in the z direction). The model is two-dimensional; all motion occurs in the x - y plane and is independent of z . The dynamical variables are the channel thickness $h(t)$ and the fluid flow speed $v(t)$ at $x = 0$ (averaged across the channel thickness h). The coordinate origin is placed midway along the length L of the channel.

2.3. Flow-Induced Vibrations of Channel Walls

Many familiar phenomena, including noises in faulty plumbing systems and sound production in the larynx and in musical wind instruments, involve the excitation of vibration by fluid flow. In such phenomena, instability can arise because an increase in fluid flow speed is accompanied by a drop in pressure through the Bernoulli effect, which causes the channel boundaries (vocal cords, woodwind reeds, etc.) to deform, contracting the channel and constricting the flow. The flow speed decreases, raising the pressure, expanding the flow channel, and raising the flow speed, and the cycle repeats.

Julian (1994) investigated the possible excitation of volcanic tremor by such a mechanism, and formulated a lumped-parameter mathematical model for the case of flow in a tabular channel such as a volcanic dike (Figure 5). This model leads to a system of third-order highly nonlinear ordinary differential equations for the temporal evolution of the channel thickness $h(t)$ and the fluid flow speed $v(t)$ at $x = 0$ (averaged across the channel thickness):

$$\rho \dot{v} + \frac{12\eta}{h^2} v = \frac{p_1 - p_2}{L} \quad (1)$$

$$\left[M + \frac{\rho L^3}{12h} \right] \ddot{h} + \left[A + \frac{L^3}{12h} \left(\frac{12\eta}{h^2} - \frac{\rho \dot{h}}{2h} \right) \right] \dot{h} + k(h - h_0) = L \left[\frac{p_1 + p_2}{2} - \rho \frac{v^2}{2} \right] \quad (2)$$

Here, t is time, ρ is the fluid density, η is the dynamic viscosity of the fluid, p_1 and p_2 are the fluid pressures in reservoirs at the upstream and downstream ends of the channel, L is the channel length, M is one-half of the mass of each channel wall per channel width, A is one-half of the damping parameter of each wall, k is one half of the elastic spring constant per channel width resisting the motion of each wall. The wall-motion parameters M , A , and k are all normalized per unit width in the z direction. Note that the since the parameters M and k are estimated per unit of channel width, they implicitly encompass another model parameter, the aspect ratio of the channel.

Numerical integration of this system gives solutions exhibiting several types of behavior, including (after an initial transient) steady flow, simple periodic oscillations, a period-doubling cascade leading to more complex periodic oscillations, and aperiodic chaotic oscillations. The prediction of period-doubling cascades was subsequently verified by observations at Mt. Semeru, Indonesia, and Arenal volcano, Costa Rica (Julian, 2000) and in laboratory models in which gas flows through tabular channels with walls of gelatine blocks or rubber sheets (Rust et al., 2008).

Julian's lumped-parameter model involves many simplifying approximations, including:

- The fluid is incompressible, and thus does not support acoustic-wave propagation
- The channel walls are rigid, though movable. That is, the source model is limited to pressure driven motion of a mass (per unit length) of the order of ρL^2 with viscoelastic resistance defined by k and A . The wave propagation away from the moving mass is considered at a later stage
- The flow-speed profile across the channel is taken to be parabolic, as in Hagen-Poiseuille flow

Rust et al. (2008) and Lipovsky and Dunham (2015) have discussed a more generalized model in which the rigid wall assumption was relaxed. At this stage of the investigation we chose to proceed with the most basic model (Julian, 1994), which encompasses quite a broad range of parameter space (see Section 2.5), only part of which is explored. A future study could encompass a more general model.

2.3.1. Tremor Onset and Duration

Julian (1994) defines the dimensionless parameters

$$r_1 \stackrel{\text{def}}{=} \frac{\rho L v_s^2}{k h_s}, \quad (3)$$

$$r_2 \stackrel{\text{def}}{=} \frac{(A + a)m}{(M + m)a}, \quad (4)$$

and

$$r_3 \stackrel{\text{def}}{=} \frac{a(A + a)}{k m}. \quad (5)$$

Here, v_s and h_s are the values of v and h in the marginally unstable state at the onset of tremor and

$$m \stackrel{\text{def}}{=} \frac{\rho L^3}{12 h_s} \quad (6)$$

and

$$a \stackrel{\text{def}}{=} \frac{\eta L^3}{h_s^3} \quad (7)$$

measure the contributions of the fluid to the inertia and damping of the wall motion. The quantity r_1 measures the kinetic energy of the fluid relative to the wall stiffness. The quantity r_2 compares the effect of the fluid upon the effective inertia and damping of the channel-wall motion. It is increased by the contribution to the inertia and decreased by the contribution to the damping. Parameter r_3 measures the total damping.

Julian (1994) then defines the stability parameter

$$R \stackrel{\text{def}}{=} \frac{1 + 2r_1}{(1 + r_2)(1 + r_3)}, \quad (8)$$

and demonstrated that sustained oscillations occur when $R > 1$ whereas chaotic behavior appears when $R \gg 1$. When $R < 1$ damped oscillations appear. The closer R is to 1 the slower the decay, and so R is a proxy for the oscillatory coda. The parameter R characterizes the behavior of the channel and therefore of the seismic source time function (Figure 6). As explained in Section 2.5 we use R as a proxy of the observed coda, which helps to narrow down a-priori the breadth of the parameter space we explore.

2.4. Parameter Constraints: Martian Magma Viscosities, Channel Dimensions, and Flow Rates

The threshold condition for the onset of oscillation in Equations 1 and 2 depends on the kinetic energy of the fluid relative to the wall stiffness, the effect of the fluid on the effective inertia and damping of the channel-wall motion, and the total damping (Equations 3–5 and 8). These depend on the parameters described in Section 2.3 as well as the fluid speed, v_s , and channel width, h_s , in the marginally unstable state at the onset of tremor.

Magma viscosity is a function of temperature, bulk composition, volatile content, the volume fraction of gas bubbles and/or crystals, and strain-rate. The effects of temperature and composition (Shaw, 1972) as well as the fraction of crystals (Marsh, 1981) are generally well understood (cf. Giordano et al., 2008a; Hui & Zhang, 2007). Mafic magma viscosities are generally smaller than the viscosities of more evolved magmas. Magma viscosity decreases with increasing water content and increases with increasing crystal fraction.

Channel dimensions and volume estimates have been used to estimate effusion rates of both aqueous flows (Burr, Grier, et al., 2002; Keszthelyi et al., 2007) and lava flows (Jaeger et al., 2010). The cross-sectional

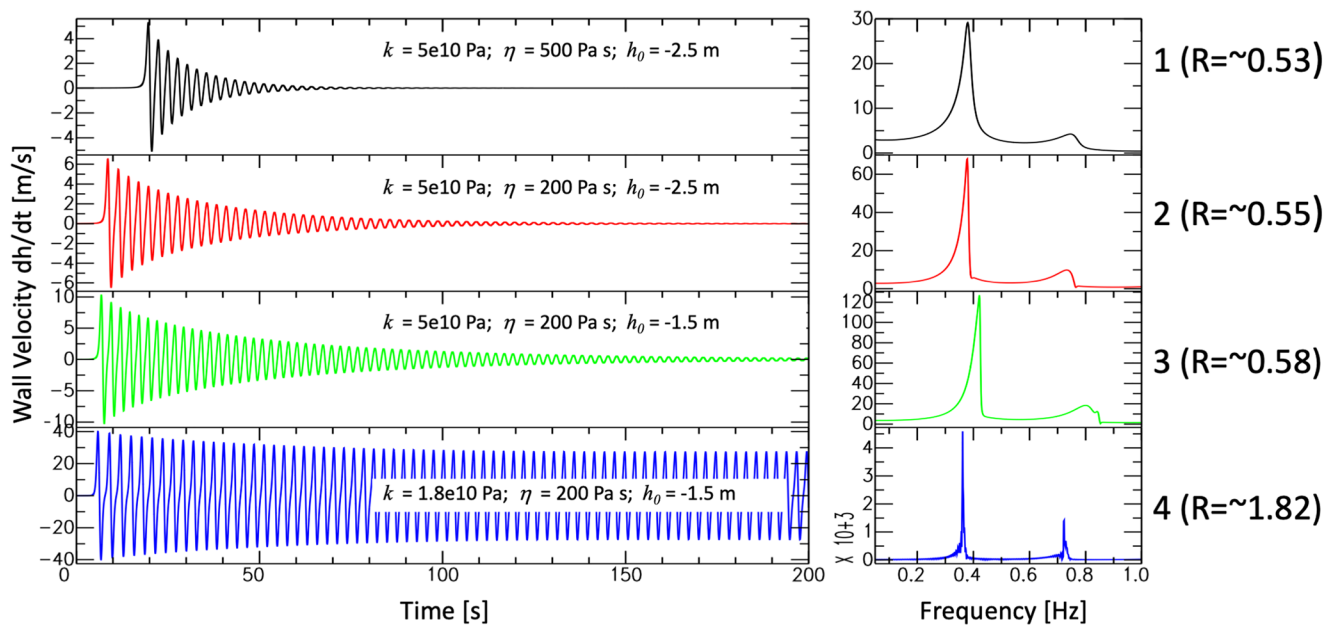


Figure 6. Four illustrative examples of different channel behaviors with varying wall elasticity k , fluid viscosity η , and equilibrium thickness h_0 . For illustration purposes, the channel length, L , its aspect ratio w/L , and the driving pressure are held constant. In this example, as the channel walls become more compliant (lower k), the fluid viscosity η is lowered, and the channel is less tightly shut (lower h_0) it becomes more conducive to sustained oscillations. As described in Section 2.5, to simulate a sustained oscillation of ~ 10 min as is the case for S0105a (Figure 2), we use an R value of 0.95 with a standard deviation of 0.05.

area of Athabasca and the inference of a single flow led Jaeger et al. (2010) to model flow emplacement as turbulent. Mineralogical maps produced by the Compact Reconnaissance Imaging Spectrometer for Mars (CRISM) instrument on board MRO tentatively identify these lavas as mafic to ultramafic in composition, consistent with the viscosities (10^0 – 10^5 Pa s) derived from modeling of adjacent plains volcanism (Vaucher et al., 2009). A mafic-ultramafic composition is consistent with the preferred viscosity value of 50 Pa s derived using a model of turbulent emplacement (Jaeger et al., 2007). Greeley et al. (2005) estimate viscosities of 2.8–50 Pa s based on picritic lava compositions measured in Gusev crater. They note that these viscosities are likely similar to Archean high Mg basalts on Earth or mare lavas on the Moon.

The Greeley et al. (2005) estimate is 1–3 or more orders lower than typical Hawaiian basalts but is plausible for ultramafic lavas. Effusion rates are estimated to be in the range of 1 – 4×10^6 m³/s for both lava and aqueous flows at Athabasca Valles (Burr, Grier, et al., 2002; Keszthelyi et al., 2007). Aqueous outflow channels on elsewhere on Mars have even larger estimated discharge rates, such the estimate of up to 10^7 m³/s at Ares Valles (Andrews-Hanna & Phillips, 2007).

Using compositions similar to anhydrous Martian nakhlites, Vetere et al. (2019) found that the melt is extremely fluid (2–8 Pa s) at temperature between 1,370°C and 1,250°C, consistent with Kolzenburg et al. (2018) who measure viscosities on the order of 1 Pa s over the temperature range of 1,230°C–1,330°C for high magnesium basalts. Adding 0.1% weight water (Filiberto & Treiman, 2009), reduces the viscosity by 18%. Using the model of Giordano et al. (2008b) with 0.1% water, the Martian basalt composition in Edwards et al. (2017) with Manganese oxide from Black and Manga (2016) yields viscosities of 3.6 Pa s at 1,300°C and 12.9 Pa s at 1,200°C.

Lava flows will have larger viscosities than the magmas that feed them due to cooling and crystallization as the lava moves across the surface, thus morphometric analyses provide an upper bound on magma viscosities at depth. Accordingly, the low magma viscosity estimates above differ from the lava flow viscosities inferred on Mars. Vaucher et al. (2009) use flow geometries across Central Elysium Planitia to estimate lava viscosities of 1.0 – 2.5×10^5 Pa s. This range of viscosities is consistent with estimates of lava rheology from morphometric analyses of Amazonian period lava flows on Mars.

Mars' reduced gravity and atmospheric pressure relative to Earth also favor deeper magma bodies and larger dike widths, effusion rates, and flow length, due to factors including smaller buoyancy forces, deeper neutral buoyancy zones, lower lithostatic pressure, and larger gas expansion (Greeley et al., 2005; Parfitt & Wilson, 2008; Wilson & Head, 1994; see also Grott et al., 2013 for a review).

2.5. Bayesian Exploration of Trade Space

Because there is a large number of parameters that can be varied in the modeling of the observed signals using the model of Julian (1994), we choose to explore the model space using a Bayesian sampling technique. We use the Markov chain Monte Carlo (MCMC) approach which is an implementation of the Metropolis-Hastings algorithm (Hastings, 1970; Metropolis et al., 1953), which has found increasing use in geophysical inversion in the past few decades (Gallagher et al., 2009; Sambridge & Mosegaard, 2002). Rather than a traditional geophysical inversion, which can use a variety of techniques to mathematically estimate a “best-fit” model and uncertainty subject to a variety of constraints, MCMC methods rely on random generation of new models within the allowed model space to which an acceptance criteria are applied such that the final population of kept models is proportional to the likelihood of the model given the observed data. We will not go through a detailed discussion of the method here, but briefly summarize that the algorithm is based on “Markov chains” of models which are created by randomly generating new models by a small perturbation to one model parameter from the previous iteration. For each model, the misfit to the observed data is calculated, and is compared to the misfit of the previous iteration to determine an acceptance probability. If the misfit is improved, the model is always kept. If the misfit becomes worse, the model may be kept with a probability that depends on the difference in misfit compared to the previous iteration. In general, this procedure is performed with multiple chains beginning from different starting models, and the final population of models can be shown to sample the model space proportionally to what is called the “posterior probability density function” (posterior PDF). In other words, there will be more models kept where the misfit is low and the probability of the model given the observed data is high, and fewer where the probability is lower. This final ensemble allows us to thoroughly explore the tradeoffs between different model parameters and how they affect the fit to the data, rather than simply arriving at a single best-fit model with uncertainties that may not show how some model parameters are correlated with each other. In this study we choose to fit the amplitude and frequency of spectral peaks within a constrained range of R values from the source model for two representative events. The parameters that we choose to fit, and the reasoning behind that choice, are described in more detail in Section 2.5.2.

2.5.1. Seismic Amplitude Estimation Methodology

Because MCMC approaches rely on estimating fit to the data for many models (thousands to millions or more, depending on the application), such methods rely on rapid computation of predicted data values for a given model. In our case, our primary seismic observations are the frequency and amplitude of the observed signals. Therefore, we need a method to rapidly estimate the seismic amplitudes generated by the wall motions predicted by the model of Julian (1994) observed at large distances from the source of the tremor. This is done in three steps: (1) Giving the Julian (1994) source a seismic moment representation; (2) Propagating the source energy from Cerberus Fossae to InSight; (3) Establishing a Moment-Amplitude scaling relationship that is then used in the MCMC process.

2.5.1.1. Translating the Oscillating Channel Source into Seismic Moment

The tremor source is determined using numerical integration of the Julian (1994) model using a range of input parameters (as discussed in Section 2.5.2). The output of this modeling is a time series of the displacement and velocity of the channel wall, as well as the fluid velocity through the channel. This is converted to a seismic source which we place at 60 km depth below the Cerberus Fossae region. A shallow 6 km depth source was also tested as a control case and is included in supplementary material. We use a moment tensor defined by an east-west oriented Compensated Linear Vector Dipole (CLVD) moment tensor source compatible with suggestions from observations of deep volcanic tremor on Earth (Aso & Tsai, 2014a). The seismic moment for an event, M_0 , is defined using the standard expression,

$$M_0 = \mu A_f d, \quad (9)$$

where μ is the shear modulus of the wall material, A_f is the area of fracture that is oscillating, and d is typically defined as fault slip, but in this case is the net motion of the wall, determined by the summed peak-to-peak motion of the wall, h , as determined from the time series output of the tremor modeling. The shear modulus μ is related to the spring constant k in Equation 2 through the relationship $k = \mu L/w$, and where $A_f = Lw$. In effect, this treats the total moment of the oscillation as a sum of alternating “sub-events” representing the channel walls moving back and forth. The area is defined by the input parameters into the tremor modeling: L , the vertical dimension of the oscillating crack, and the aspect ratio to the long dimension of the crack, which is used to define the wall stiffness, k , in the modeling. Finally, we convolve the seismogram with a source-time function defined by the model output wall velocities, \dot{h} (Figure 6), normalized by the integral of the absolute value of wall velocity, which is the appropriate normalization for an oscillatory source. Note that normalization by the integral of the absolute value of wall velocity is needed because the “sub-events” discussed above alternate in direction, leading to a wall velocity oscillating between positive and negative (Figure 6). Without using the absolute value, the integral of such a function approaches zero and normalizing by that integral would incorrectly amplify the source by orders of magnitude.

2.5.1.2. Propagating the Seismic Energy

In order to compare amplitude predictions from a tremor source at Cerberus Fossae with the observed seismic amplitudes at the InSight landing site, we need to propagate seismic waves from a predicted source to the InSight landing site. We do this using Instaseis (van Driel et al., 2015), a flexible tool for rapidly generating seismograms for arbitrary source and receiver configuration based on databases computed with the 2D axisymmetric spectral element wave propagation program AxiSEM (Nissen-Meyer et al., 2014). For this study, we use databases already calculated for a priori models of Mars structure for a blind test for the mission's Marsquake service (Ceylan et al., 2017; Clinton et al., 2017). Many models were included in that study. We bracket the range of possible source strengths by using four models with a broad range of crustal and mantle structures. Two have identical mantle structure, but differing crustal structures: an unrealistic single layer crust (EH45Tcold), and another with a low-velocity regolith layer at the surface (EH45TcoldCrust1b). Both of these models have the same mantle structure defined by an enstatitic composition and a chosen thermal profile (Clinton et al., 2017; Rivoldini et al., 2011), but the mantle velocity structure has a small effect on the amplitude compared with the shallow crustal velocity structure. We also choose two models with a different mantle structure with less of a negative shear velocity gradient, which is necessary to produce an observable S-phase in the distance range compatible with Cerberus Fossae. These two models (DWAK and TAYAK, Clinton et al., 2017) are calculated using the methodology of Khan and Connolly (2008). An example of the calculation of seismic amplitudes for a given tremor model is illustrated in Figure S1 of the Supplementary Material.

One critical shortcoming in this approach is that it is based on 1D seismic velocity models which inherently ignore the effects of scattering due to 3D velocity structure. This type of scattering appears to be an important feature of Mars seismograms observed to date (Lognonné et al., 2020). In particular, the seismograms computed with Instaseis (see Supplementary Material) show strong polarization separating the coupled P and SV (vertically polarized shear) waves from SH (horizontally polarized shear) waves. The largest amplitudes also represent surface wave energy (Rayleigh and Love waves) which are also not observed in Mars data to date (Lognonné et al., 2020), which may also be related to strong scattering. This scattering will likely affect the duration of the seismic energy arrival energy, and also adds significant uncertainty to the amplitudes. For periods between 1 and 10 s (relevant to the signals discussed here), amplitudes due to 1D surface waves may be overestimated by up to 1 order of magnitude (e.g., Panning et al., 2020), although this should not impact the frequency content. For this reason, we decide to focus on root mean squared (RMS) body wave amplitudes calculated between the predicted P and SS arrivals in order to remove the influence of surface waves when comparing with actual InSight data. Because scattering should not impact the frequency content from the source, the amplitude is the only remaining impact on our Bayesian model fitting. With the exclusion of surface wave energy, the uncertainty due to amplitude perturbation from 3D scattering is likely comparable to the uncertainty already present due to uncertainty on the velocity model for propagation.

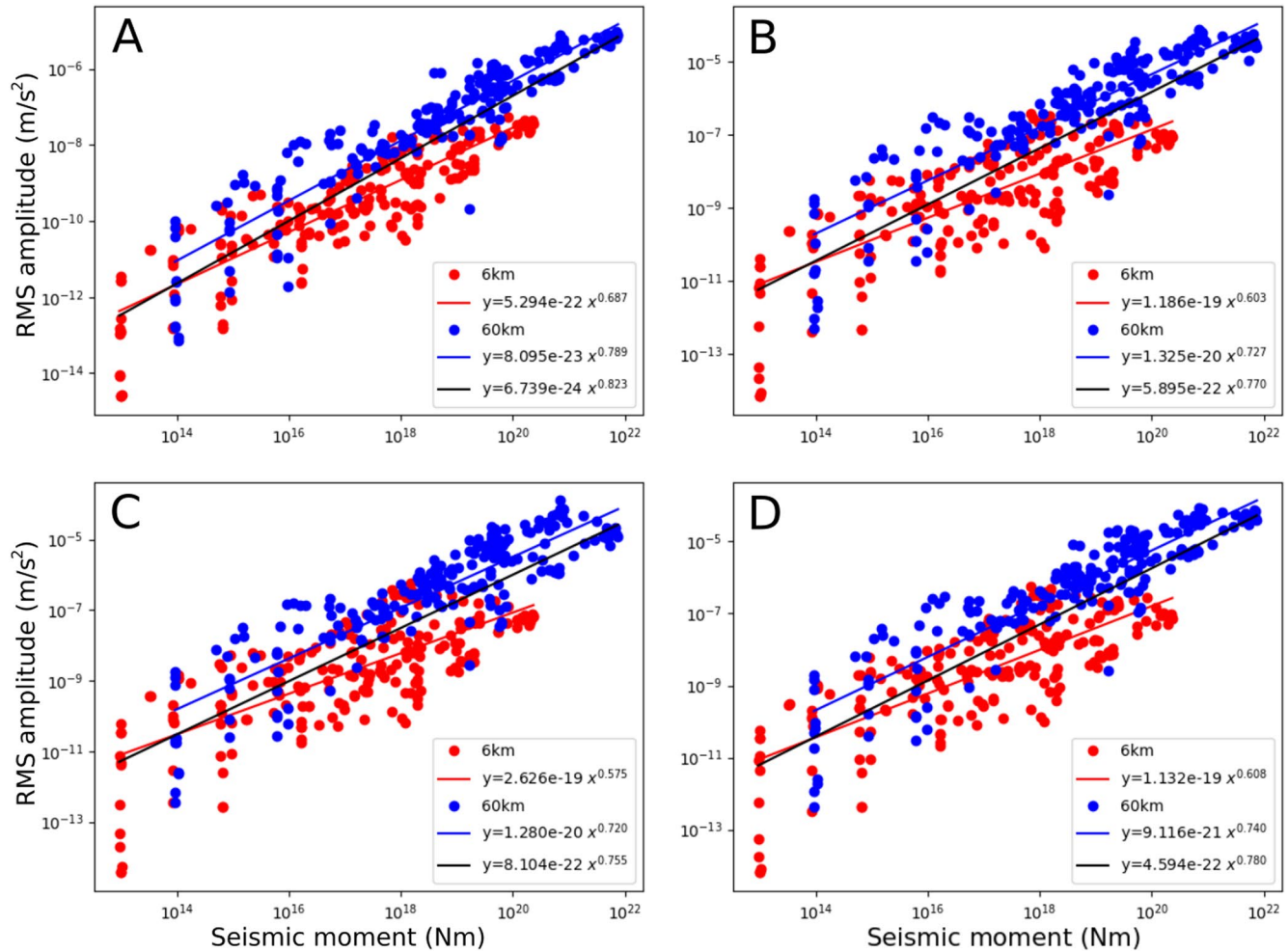


Figure 7. Calculated root mean squared vertical amplitude calculated over a the time window between predicted P and SS arrivals compared with calculated seismic moment from the tremor model output for a range of input models described in the text. Results are shown at depths of 6 km (red), and 60 km (blue). Best power law fits are shown for each depth individually (red, blue, and green lines), as well as across all depths (black line). Fits are computed separately for velocity model EH45Tcold (a), EH45TcoldCrust1b (c), DWAK (b), and TAYAK (d).

2.5.1.3. Moment-Amplitude Empirical Scaling Relationship

Finally, in order to speed up the calculation for a single model to enable Bayesian parameter space exploration and to ensure a smooth variation of amplitude as a function of tremor model input parameters, we calculate an empirical scaling relationship between the calculated seismic moment and modeled seismogram amplitude (Figure 7). Seismic amplitude in this case is defined by the root mean squared average of the vertical ground acceleration amplitude over a body wave time window that excludes surface wave energy.

Models in Figure 7 are calculated over a wide range of parameter combinations varying L from 50 to 600 m, pressure ratio between 0.1% and 10%, aspect ratio between 5 and 50, and viscosity ranging from 0.01 to 780 Pa s. These models are sampled in a regular grid within those parameter ranges, and tremor sources are calculated with the Julian (1994) model, and then used as seismic sources in AxiSEM numerical wave propagation simulations. RMS averages of seismic amplitudes within a body wave window between predicted P and SS arrivals are then calculated for each possible combination of model parameters within the grid, and plotted in Figure 7. Scaling ratios between calculated seismic moment derived from the Julian (1994) model and the amplitude calculated from the synthetic seismograms are then defined so that the wave propagation code is not needed for every model generated in the Bayesian exploration. We would expect a linear relationship between moment and amplitude observations. However, the observed relationship deviates from linearity due to covariance between fault dimensions and tremor source frequencies and other

source characteristics. All models show a similar slope as a function of moment and a similar separation between the shallow and deep source, with the deep source showing consistently higher amplitude, which is due to seismic amplification when the source is placed in an elastically stiffer layer than the surface, which is less pronounced for the shallow source. A similar calculation where amplitudes are calculated using the synthetic surface wave amplitudes (supplementary Figure S2) does not show a significant offset between sources at different depths, as the amplification effect is compensated by reduced excitation of surface waves by deeper sources. Given this offset in the amplitudes as a function of depth, the following modeling uses the amplitude scaling relationships calculated for the specific depth of the source. We also explored placing depths down to 150 km (not shown here), which may represent the deepest depth from which magma may be originating (Grott et al., 2013) but saw very similar amplitude scaling as for the 60 km source depth, due to relatively small variations in predicted shear modulus across that depth range. Also note that models DWAK, EH45TcoldCrust1b, and TAYAK (Figures 7b–7d) show very consistent amplitudes, while EH45Tcold (Figure 7a), which has the highest velocity crust, and therefore the smallest amplification effect, shows magnitudes lower by approximately one order of magnitude.

2.5.2. Parameters for MCMC Exploration

Of the range of model input parameters discussed in Julian (1994) and in Section 2.3, we choose to vary five key parameters in the MCMC exploration:

- L , the channel length (vertical dimension in Figure 5). This is the most important parameter for determining the frequency of oscillation. It is allowed to vary between 1 and 1,000 m
- η , the viscosity of the fluid. In order to consider a range of possible sources ranging from hydrothermal activity to magma motion into dikes, we allow this to vary between 8.9×10^{-4} Pa s (the viscosity of water at standard temperature and pressure) up to 1,000 Pa s to span the range typical of basaltic magmas
- p_2/p_1 , The driving pressure ratio. p_1 is defined by the lithostatic pressure at the depth of the source, and we allow an overpressure driving flow ranging from 0.001% to 20%
- w/L , The aspect ratio of the channel, where w represents the along-strike dimension of the crack shown in Figure 5. This controls the elastic stiffness of the walls, which is defined as $k = L\mu/w$ (Julian, 1994), where μ is the shear modulus of the wall material at the depth of the source. We allow this ratio to vary between 5 and 100
- h_0 , the equilibrium crack opening. Because this is happening at depth, we assume the crack is under pressure and therefore has a negative value for equilibrium crack opening. We assume any flow is episodic, given that we do not see continuous excitation of the vibration, and therefore the equilibrium opening width is close to the critical value at which oscillation is no longer possible (Julian, 1994), defined as $h_{0,\text{crit}} = -(p_1 + p_2)L/(2k)$. In the exploration, we allow h_0 to vary between 0.9 and $0.99 \times h_{0,\text{crit}}$

We explore sources at two depths, (6 and 60 km), but for the reasons described in Section 1.1 we focus on the deeper source location here, with the shallower source results shown in supplementary material. Other parameters fixed in the modeling are described in the README file in the data repository at <https://github.com/mpanning/tremor> (doi: 10.5281/zenodo.4519818). This included defining the standard deviations of model parameter perturbations, which can control the rate of convergence of the MCMC modeling. Additionally, the gravity of Mars is taken into account for the lithostatic pressure calculations, but has little impact on the seismic wave propagation except at very low frequencies below our range of interest.

Finally, we performed MCMC Bayesian inversions attempting to match the amplitude and the frequency of S0105a and S0189a (Figure 2), whereas the allowable model parameter space is constrained by the parameter R as described in Section 2.3. This involved creating a data vector with the dominant period of observation, set to 2.86 s (0.35 Hz) for the S0105a event or 1.67 s (0.6 Hz) for S0189a event, with standard deviation of each set to 17.5% of the period (0.5 s for S0105a and 0.3 s for S0189a); the amplitude of the signal, set to 1.5×10^{-9} m/s² for S0105a and 1.4×10^{-9} m/s² for S0189a, with standard deviation of 0.5×10^{-9} m/s². Since the observed signal has a finite (~15 min) duration in the sense that it does not oscillate indefinitely, but also does not die out in only a handful of cycles. Based on Julian (1994), this is typical of models with the dimensionless R value (Equation 8) just less than 1. We incorporate this by adding a third element to the data vector setting the R value to 0.95 with a standard deviation of 0.05. We choose to focus on two of the considered velocity models (TAYAK and EH45Tcold), as the other two models had amplitude scaling similar to TAYAK. We performed four sets of MCMC inversions for the combination of the two velocity models

and the two possible source depths (6 and 60 km). Each chain is initiated with a random model selected from a uniform distribution between the limits described above. Model perturbations, however, are selected from a log-normal distribution for all parameters except fraction of h_0 . For each inversion, we ran at least 33 chains with 10,000 iterations each. The first 1,000 models were discarded as burn-in, while every 10th model after that was saved to the model ensemble in order to have them be independent samples.

In the inversion process, the misfit ϕ is defined as the normalized sum of the squared errors,

$$\phi = \sum_{i=1}^3 \frac{(x_i - x_{i,\text{pred}})^2}{\sigma_i^2}, \quad (10)$$

where i is an index over the three observations (amplitude, frequency, and R value), x_i and $x_{i,\text{pred}}$ are the observations and model predictions, respectively, and σ_i is the assigned standard deviation for each data value described above. Convergence of misfit values was typically reached within the burn-in period, and the remaining model iterations explored the low misfit space (Figure S10).

3. Results and Interpretation

3.1. Results of Bayesian Exploration

In an MCMC inversion, histograms of parameters from the final model ensemble are proportional to the probability density function for that parameter. This allows us to look at the likelihood of a value for a particular parameter (Figure 8) or for tradeoffs between model parameters (Figures 9 and 10). Parameters for many input and derived model parameters are available in the supplementary material, but we choose to focus on a few key parameters and tradeoffs. As an important caveat, some chains failed to converge to fits within three sigma of the data, and so for the plots, only models with frequencies between 0.2 and 0.6 Hz for S0105a and 0.3–0.9 Hz for S0189a and R values between 0.8 and 1.1 are plotted. For the shallow depth (Figures S3 and S4), both models show very consistent results, despite the large amplitude difference, but there is a large divergence between the models for the deeper source (Figure 8). In general, however, the results are similar for the two different events considered, despite the difference in resonant frequency, except for the L parameter, which is peaked around 140 m for S0105a and near 90 m for S0189a (Figure 8).

L is, in general, tightly constrained relative to the prior range (Figure 8). This is the primary parameter controlling the frequency of the oscillation, and so this is tightly constrained for a given frequency of observation. Note that the frequency of LF events we interpret as potential tremor signals varies between events, and therefore this model would require different cracks to be activated for different events, which might indicate a plexus of dikes in the source region. This is to be expected considering differences in epicentral distance and variation of along-long strike widths of Cerberus Fossae fissures.

Viscosity differs significantly between the two depths considered. At the shallower depth (6 km), most models have viscosities between 10 and 1,000 Pa s regardless of seismic velocity model used (Figure S5), which are reasonable basaltic magma viscosities, and most models favor viscosities at the high end of the considered range. This same characteristic remains for the EH45Tcold model at 60 km depth for both candidate tremor events (red-toned bars in Figure 8), while lower viscosities mostly between 1 and 10 Pa s for S0189a (cyan bars) and between 0.1 and 1 Pa s for S0105a (blue bars) are favored when using the TAYAK velocity model (blue-toned bars in Figure 8). For the S0189a events, this is consistent with the lowest estimated basaltic magma viscosities, while the S0105a is more intermediate between the lowest viscosity magmas and water. Calculations with amplitudes not removing surface waves (which are therefore larger for a given source model) were also broadly consistent with this for S0105a (Figure S2 in supplementary material), although favoring somewhat lower viscosities at both depths. The EH45Tcold model at depth, however, shows a very different result with viscosities peaking around 100 Pa s, more typical of basaltic magmas.

The equilibrium crack opening also varies between the two depths. At the shallow depth, a wide range of values are possible, but values above $0.98h_{0,\text{crit}}$ are not likely (Figure S5 in supplementary material). For the 60 km models which are the focus here, though, both events and structure models are mostly clustered around the higher values (meaning a more strongly clamped initial crack). Some chains did produce models with less clamping, but most of these were excluded by the filtering of models which did not fit frequency or

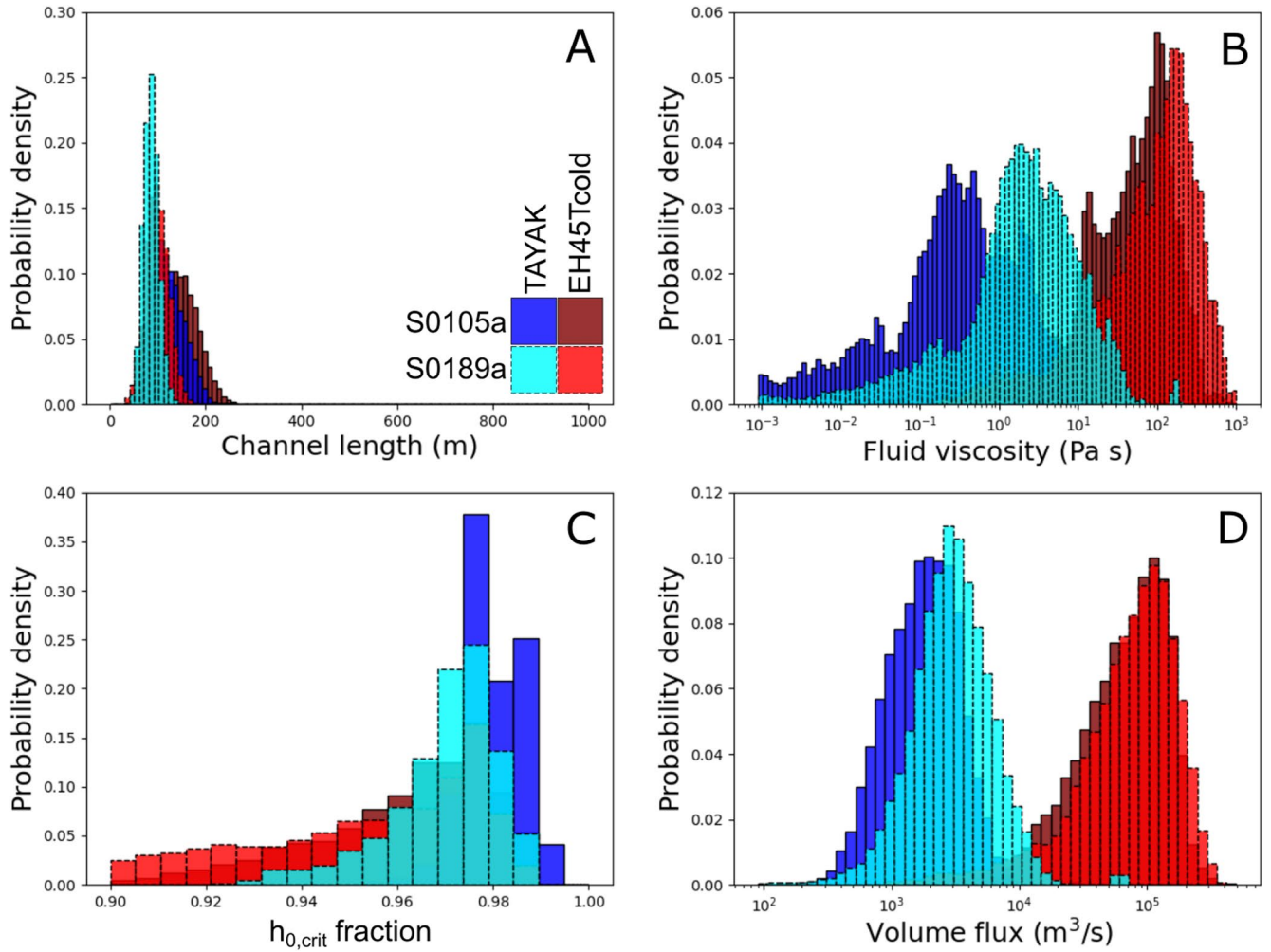


Figure 8. Probability density functions (PDFs) for MCMC model ensembles for a source placed at 60 km depth. Results are shown for the combination of two events S0105a in darker colors and S0189 in lighter colors; see legend in panel (a) and two models (EH45Tcold in red tones and TAYAK in blue tones). PDFs are plotted for the vertical crack length (L) (a), viscosity (η) (b), the fraction of $h_{0,crit}$ (c), and the volume flux (d). PDF, Probability density function.

R values within three sigma. This implies that the channel tends to be strongly clamped. We can speculate that under such conditions a channel would open for brief periods but would mostly remain shut. We can further contemplate that events with less tightly clamped channel might be more readily excited yet would produce a weaker and likely shorter signal.

Because the geometry and flow velocity of the fluid are defined by the model input and outputs, we can also look at derived quantities like fluid volume flux in order to assess how reasonable the obtained solutions are. We derive this using the crack width w , and predicted steady crack opening, h_s , and flow velocity, v_s , which is defined in Julian (1994) as the solution to the coupled equations

$$\frac{12\eta}{h_s^2} v_s = \frac{p_1 - p_2}{L} \quad (11)$$

$$k(h_s - h_0) = L \left[\frac{p_1 + p_2}{2} - \frac{\rho v_s^2}{2} \right]. \quad (12)$$

The steady state volume flux is then defined as $F = h_s \times v_s \times w$. In this case, we see a big difference in acceptable models depending on the choice of structural model. For EH45Tcold (with the simplified relatively high velocity crustal model), the accepted flux values are all near $10^5 \text{ m}^3/\text{s}$, while the TAYAK model (which

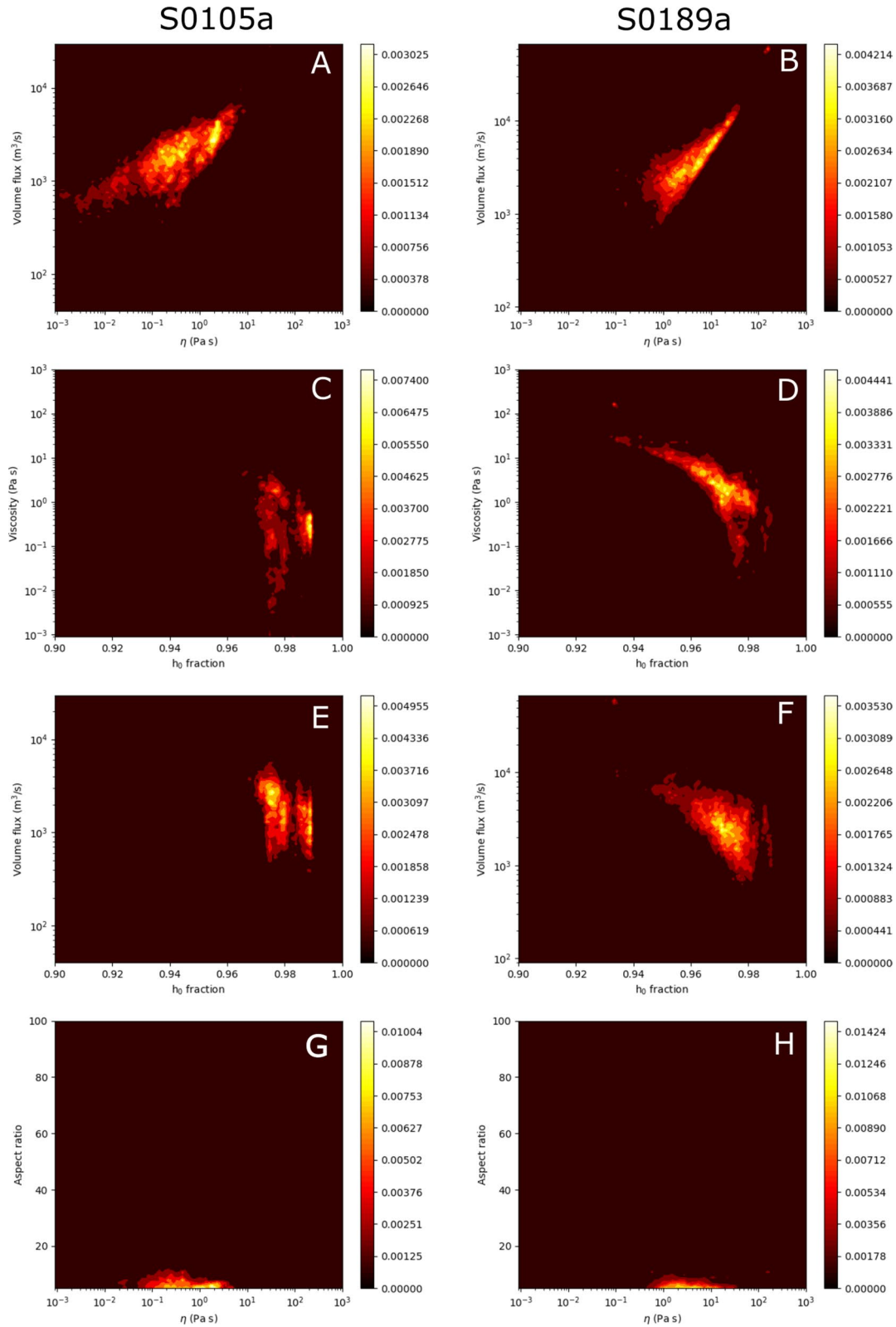


Figure 9. Two-dimensional plots of probability density functions (PDFs) comparing model parameters for MCMC model ensembles for the S0105a event (left) and the S0189a event (right) calculated with amplitude scaling from the TAYAK model. Color scale represents probability density comparing viscosity (η) and volume flux (a) and (b), fraction of $h_{0,\text{crit}}$ and viscosity (c) and (d), fraction of $h_{0,\text{crit}}$ and volume flux (e) and (f), and viscosity and aspect ration (g) and (h). PDF, probability density function.

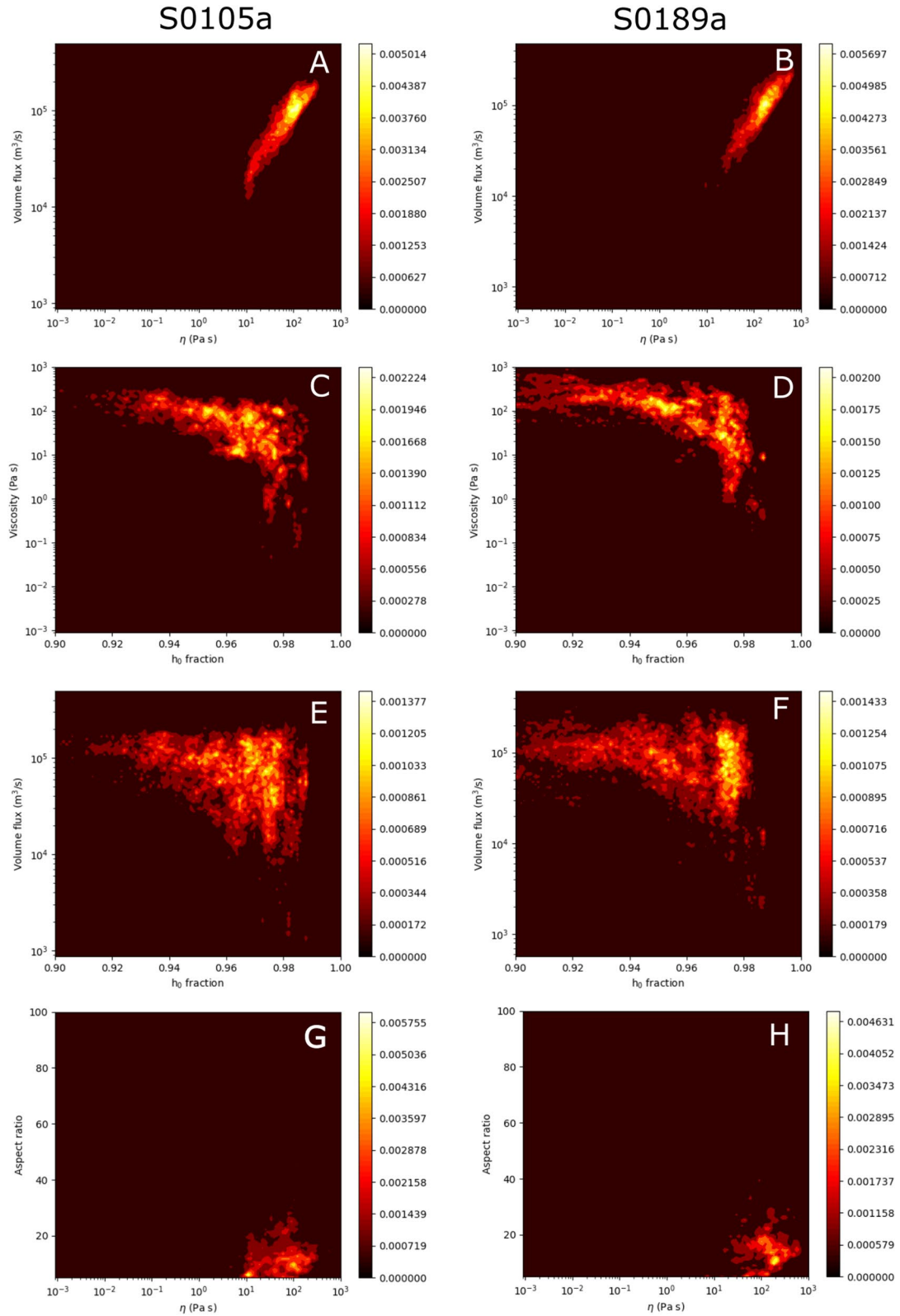


Figure 10. Same as Figure 9, but using the amplitude scaling relationships calculated for the EH45Tcold model.

produces amplitudes consistent with other tested models with more realistic crustal velocities) shows much lower fluxes between 10^3 and 10^4 m³/s. Both events, however, show consistent results with each other for a given structural model. To put these fluxes in perspective, the mean volume flux of the river Seine in Paris is ~ 500 m³/s, and so even the lower fluxes for the TAYAK model represent a significant flow rate, but the flow may only occur for ~ 10 min at a time to match the observed tremor durations, which would end up producing a total volume flow of between 10^{-3} and 10^{-1} km³ for the range of models shown here. This is a large volume of material, but relatively small compared to volumes of large volcanic eruptions. For example, it is roughly one to three orders of magnitude smaller than the eruptive volume of the 2018 Lower East Rift Zone eruption at Kilauea (Neal et al., 2019) and two to four orders of magnitude smaller than the 1,980 Mount St. Helens eruption, and many orders of magnitude smaller than the volume of large flood basalts observed on Mars. For the 6 km models (Figure S5), both events and structural models require larger volume fluxes comparable with the EH45Tcold model results at the 60 km depth.

The largest historical basaltic lava flow on Earth, the 1,783 Laki eruption in Iceland, had a peak eruption rate of 8.7×10^3 m³/s (Thordarson & Self, 1993). Eruption rates at Mauna Loa, Hawai'i, compiled by Wadge (1981), are less than a couple hundred m³/s, similar to the most recent 2018 Kilauea eruption of 130–200 m³/s (Neal et al., 2019). The peak eruption rates at Mauna Loa reached 1.5×10^3 m³/s in 1950 and 800 m³/s in 1984 (Lipman & Banks, 1987). Other large historical eruptions have similar or smaller eruption rates, including 2014–2015 Holuhraun, Iceland (Pedersen et al., 2017). It is not obvious that the much larger 10^4 km³ prehistoric flood basalt lavas had much larger eruption rates. If flood basalt lavas are large pahoehoe flow fields (Self et al., 1996), then average eruption rates would be less than 10^4 m³/s (Self et al., 1997). Models of thermochronology (Karlstrom et al., 2019) and the extent of thermal alteration (Petrovic & Dufek, 2005) of rocks adjacent to feeder dikes provide similar maximum eruption rates of less than 6×10^4 m³/s for Columbia River flood basalts.

While surface eruption rates cannot be directly compared to flow rates of magma at depth, they do provide context to the flow regime and magma properties. Larger eruption rates have been inferred on Mars using models to interpret flow geometries and morphologies. Keszthelyi et al. (2000) suggest that recent flood lavas in Central Elysium Planitia had average eruption rates of 10^4 m³/s, with surges up to 10^6 m³/s, and Vaucher et al. (2009) inferred similar but slightly higher fluxes of 2×10^4 and 8×10^4 for the largest flows. Grosfils et al. (2000) inferred rates up to 10^4 m³/s in Marte Vallis. Cattermole (1987) inferred larger eruption rates of 10^6 m³/s for the early flood lavas at Alba Patera. Wilson & Head III (1994) argued based on theoretical arguments that effusion rates on Mars would be five times larger than on Earth.

3.1.1. Parameter Trade-off

One strength of Bayesian approaches like MCMC is that we can also explore tradeoffs between model parameters (including both input and output parameters) to fit the data equally well through two dimensional plots of the probability density function sampled by the final model ensemble. The most prominently correlated parameters in our data set are volume flux and viscosity (Figures 9 and 10, top row). There is a strong positive correlation between these quantities. However, the dominant effect appears to be that models that produce sufficient oscillation amplitude at higher viscosities require greater crack opening widths, which leads to larger net volume fluxes. The driving pressure is not a well-constrained parameter, and so it does not have a strong impact on the feasibility of the tremor models, and no apparent correlation with flux (See Figure S8).

We also see a weak negative correlation between equilibrium crack opening fraction and viscosity for all combinations of modeled structure and event, except for the TAYAK model for S0105a which sees very little variation in accepted equilibrium crack opening fraction (panel C in Figure 9). Keeping in mind that larger crack opening fractions correlate to more negative h_0 values, which would be more clamped off to start with, this indicates that lower viscosities are required in order to generate sufficient flow when the cracks are more clamped off, which is more consistent with expectations. However, the lower values of equilibrium crack opening fraction (less than 0.95) do not show as clear of a correlation with viscosity for the EH45Tcold model (Figure 10c and 10d).

Given the clear positive correlation between viscosity and volume flux and somewhat negative correlation between h_0 fraction and viscosity, we would expect to also see a negative correlation between h_0 fraction and

volume flux. However, the relationship is not quite so clear. Higher volume flux models are accepted at all h_0 fractions, but the lowest fluxes in each combination of structure model and event are associated with the most clamped cracks (largest h_0 fractions).

For both velocity models, there is a positive correlation between viscosity and preferred aspect ratio of the crack at the 6 km depth (Figures S6–S7), which would indicate that the higher viscosity models require much larger aspect ratios, and thus larger crack cross sections, contributing to the strong correlation between viscosity and volume flux. At 60 km depth, however, all models for the TAYAK structure model have aspect ratios near the minimum allowed value of 5. There is a faint positive relationship between viscosity and aspect ratio for the EH45Tcold, contributing to the clearer and steeper viscosity and flux relationship observed for that model compared with TAYAK which shows a more distributed and less steep viscosity-flux relationship.

Overall, these modeling results indicate that a tremor model for a handful of apparently monochromatic events thought to originate in the Cerberus Fossae region cannot be ruled out, even though we would do not see such signals at large distances on Earth (largely due to the higher background noise from Earth's oceans and atmosphere). Models that can match the data do require generally quite large volume fluxes, which may be problematic since we are not seeing active ongoing surface eruptions. However, since magma motion at depth need not be necessarily associated with surface eruption, and since there are geologically recent flows in the area with episodic effusion rates that encompass our model results, these cannot be ruled out. The lowest volume fluxes, which could be preferred based on the lack of ongoing surface eruptions, are for the more realistic crustal model used by TAYAK, but these are also associated with viscosities that are clustered at the lowest end of realistic viscosities (0.1–1 Pa s) with many models extending to values below 0.1 Pa s that are likely unrealistically low for basaltic magma, yet still higher than expected for hydrothermal fluids. Another concern for realism of the modeling is that the model not violate the assumptions to have laminar as assumed in the Julian (1994) model. For a rectangular crack like this, we need to consider the Reynolds number, defined as

$$\text{Re} = \frac{\rho v_s D_H}{\eta_s}, \quad (13)$$

where $D_H = 4wh_s/(2w + 2h_s)$, or 4 times the cross sectional area of the crack divided by its perimeter, is the effective length scale of rectangular duct flow. The condition for laminar flow is $\text{Re} \times D_H/L < 48$. This condition is maintained for nearly all accepted models at 60 km depth, and most models at 6 km depth (Figure S9). This suggests that a tremor source is possible and not physically inconsistent but requires models closer to the turbulent flow threshold at shallower depths, which in conjunction with the lack of surface waves and of active volcanism favors the deeper source model.

3.2. Implications of Results: Could Some Mars Seismic Events be Generated by Fluid Flow Induced Seismicity?

Young volcanic and water flows, less than 10 m.y. old, are surprising on a planet where the majority of the surface has an age of 3–4 G.y. The thermal evolution of Mars can be constrained based on estimates of the elastic lithospheric thickness over time, compositional information, and interior structure (Plesa et al., 2018). Attempts to model recent volcanism rely on localized variations in heat flow, such as due to a mantle plume or higher concentrations of radiogenic elements, and relatively high water content. For a plausible assumption about geochemistry and water content Plesa et al. (2018) find that the solidus might be exceeded at depths below 200 km only in areas with a mantle plume at depth. Kiefer and Li (2016) find a similar result for an assumption of 200 ppm of water. Using the thermal model of Hauck and Phillips (2002), Schools and Montési (2018) find melting possible with 250 ppm water. There is no direct evidence, such as from gravity data, for a mantle plume beneath Elysium Mons. Cerberus Fossae sits on the volcanic plain associated with Elysium Mons (Figure 1). While it is unclear why volcanism would be so localized only at Cerberus Fossae, which is located ~1,000 km from Elysium Mons, long distance (>1,000) km transport in dikes is documented on Earth (Ernst et al., 2001). Other mechanisms, such as regional variations in lithosphere and upper mantle composition may also contribute to localized melting (Ruedas & Breuer, 2017).

The extensional fault system of Cerberus Fossae appears to be important in facilitating recent volcanism. On Earth, volcanic tremor typically occurs either near the Moho where magma tends to be trapped beneath less dense crust (Aso & Tsai, 2014b) or in shallower conduits between magma chambers and the surface. Non-volcanic tremor at plate boundaries could be caused by shear failure on a critically stressed fault in the presence of near lithostatic pore pressure as suggested by Thomas et al. (2009), and at subduction zones accompanying slow slip events (Shelly et al., 2007). Tremor is also found at plate boundaries where faults provide a conduit for fluids. The faults at Cerberus have clearly facilitated flow of both magma and water to the surface, and are likely to do so at depth as well.

Given the geologically recent volcanism at Cerberus Fossae, it is highly plausible that there is a significant volume of cooling magma at depth, either in the form of a magma chamber or possibly smaller intrusive bodies. As indicated by Vaucher et al. (2009) some of the most recent lavas in Central Elysium Planitia may be among the most fluid, consistent with the formation of magma at large depths with a small fraction of partial melt characterized by low Si abundance. Aso and Tsai (2014b) have shown that cooling magma can produce significant strain rates and LP seismic events on Earth with characteristics similar to those observed by InSight. Analysis of available geochemical data from meteorites, in-situ data, and remote sensing finds that magma chambers are likely to occur at depths of 80–150 km (see Grott et al., 2013 for a review). Like global thermal evolution models, these values may not pertain to Cerberus in particular. However, they are generally consistent with our parameter space which shows that fluid flow at a depth of 60 km could generate the observed seismic frequency content, amplitude and duration.

Water, or a combination of water and ice, can flow at shallow depths. At Cerberus evidence for both recent volcanism and water on the surface points to magma or cooling magma as the heat source driving subsurface water motion. Our analysis precludes low viscosity fluids, water, at 6 km as an explanation for S0105a and S0189a (see Supplementary material). The question is then how deep might water be capable of producing a flow and a tremor-like signature? This question is an area of active research for the Earth. Tao et al. (2020) find evidence of hydrothermal circulation and related small quakes on the Southwest Indian ridge at depths of up to 15 km, roughly 6 km below the Moho at that location. The interface at 10 km detected by SEIS may reflect the depth of a highly fractured crustal layer (Lognonné et al., 2020), and significant pore space is likely to extend tens of km deeper (Clifford & Parker, 2001). However, the tremor model analyzed here describes fluids in a conduit formed by volcano-tectonic processes, not for flow in available pore space. This mechanism may play a role if the tremor is non-volcanic in nature (Thomas et al., 2009), and should be explored in future studies. As discussed, the 1,200 km long Cerberus Fossae fault system appears to be locus of fluid flow. The depth of the overall fault system is not constrained.

4. Conclusions

Seismology is a proven powerful tool in the study and analysis of terrestrial magmatic systems. It has been used for decades to identify magmatic bodies and study their dynamics, and has been used time and again to monitor and track volcanic activity in a wide range of geological settings. In this paper, we set out to use some of the tools that have been successfully applied on Earth in a new setting, Mars. The limitations of having a single station and low Martian seismicity make this task exploratory in nature, especially at this early stage in the lifetime of the first seismometer on the Martian surface. These limitations are further compounded by the breadth of geological settings and phenomena that magmatic systems present.

We set out to explore one explanation out of many for LF seismic events in the young volcanic region of Cerberus Fossae, and examined the possibility that two LF seismic events (S0105a and S0189a) traced to Cerberus Fossae may be generated by fluid flow through a channel at depth. This hypothesis was motivated by the fact that Cerberus Fossae is a surprisingly young volcanic region, which InSight data has demonstrated is tectonically active as evidenced by the largest LF family events (S0173a and S0235b) recorded on the planet to date. The hypothesis was further motivated by the fact that some atypical LF events located at Cerberus Fossae share key characteristics with LP quakes that are common on Earth's volcanoes. We tested this hypothesis by invoking a traditional volcanic source model (Julian, 1994) in which pressure-driven fluid flows across a channel causes the channel to temporarily oscillate, and use the model properties to explore the source parameters that best fit the events' key features (dominant frequency, duration, and amplitude).

We then analyze whether key resultant source model properties (viscosity and volume flux) are reasonable given the geological history of Cerberus Fossae. We find that the model can produce the observed seismic signature, with combination of very low-viscosity magma and high volume flux of $\sim 10^3\text{--}10^5\text{ m}^3/\text{s}$ that are within an order-of-magnitude agreement with Cerberus Fossae lava flow properties deduced from analysis and modeling of regional lava flows morphologies.

It is impossible at this stage of the InSight mission, however, to conclude whether or not this is a likely explanation for Mars. The model results in fluxes that are extreme for Earth yet are just within bounds of what has been inferred for Mars and particularly for Cerberus Fossae. The volumes and inferred viscosities and effusion rates of the most recent lava flows found on Mars are substantially different than on Earth, and we should be careful not to draw far reaching conclusions based on our acquaintance with terrestrial volcanism. We therefore conclude that we cannot rule out active fluid flow as the mechanism responsible for some of the LF events that likely originate from Cerberus Fossae. It follows that our analysis does not preclude the possibility that Cerberus Fossae is underlain by a deep active magmatic system. This remains an intriguing possibility that has far reaching implications for the state and depth of magma beneath the Martian crust. Nevertheless, even though our analysis did not result in a definitive answer to the question “Are some LF events volcanic quakes?”, it greatly narrowed down the physical parameter space that allows these quakes to be volcanic and reduced it to a very specific scenario of low-viscosity, high flux events. Future studies that further explore this hypothesis, will have to take that into consideration. The physical process studied here will be either sharpened or discarded as InSight continues to collect seismic data, by future missions that might focus on Cerberus Fossae, and as alternative models are explored.

Data Availability Statement

InSight seismic data presented here (InSight Mars SEIS Data Service, 2019) is publicly available through the Planetary Data System (PDS) Geosciences node, the Incorporated Research Institutions for Seismology (IRIS) Data Management Center under network code XB and through the Data center of Institut de Physique du Globe, Paris (<http://seis-insight.eu>). Code for calculations is available via github (<https://github.com/mpanning/tremor/releases/tag/1.1> <https://doi.org/10.5281/zenodo.4519818>). The authors thank Matt Haney from the USGS Alaska Volcano Observatory for his help on Aleutian arc volcanic tremor data. The authors also wish to thank Phil Dawson of the USGS Volcano Hazards Program for a thorough review. Special thanks to the reviewers for their thorough review and input. This is InSight Contribution Number 98. Copyright 2021. All rights reserved.

Acknowledgments

S. Kedar, M. P. Panning, S. E. Smrekar, M. P. Golombek, and W. B. Banerdt were supported by the NASA InSight mission and funds from the Jet Propulsion Laboratory, California Institute of Technology, under a contract with the National Aeronautics and Space Administration. S. D. King was supported by the NASA InSight mission. The French authors acknowledge CNES and ANR (ANR-14-CE36-0012-02 and ANR-19-CE31-0008-08) for their support. The authors acknowledge NASA, CNES, partner agencies and Institutions (UKSA, SSO, DLR; JPL, IPGP-CNRS, ETHZ, IC, MPS-MPG) and the operators of JPL, SISMOC, MSDS, IRIS-DMC, NIED Hi-net, and PDS for providing SEED SEIS data.

References

- Aki, K., Fehler, M., & Das, S. (1977). Source mechanism of volcanic tremor: Fluid-driven crack models and their application to the 1963 kilauea eruption. *Journal of Volcanology and Geothermal Research*, 2(3), 259–287. [https://doi.org/10.1016/0377-0273\(77\)90003-8](https://doi.org/10.1016/0377-0273(77)90003-8)
- Aki, K., & Koyanagi, R. (1981). Deep volcanic tremor and magma ascent mechanism under kilauea, hawaii. *Journal of Geophysical Research*, 86(B8), 7095–7109. <https://doi.org/10.1029/jb086ib08p07095>
- Andrews-Hanna, J. C., & Phillips, R. J. (2007). Hydrological modeling of outflow channels and chaos regions on mars. *Journal of Geophysical Research*, 112(E08001). <https://doi.org/10.1029/2006JE002881>
- Ardid, A., Vera, E., Kelly, C., Manga, M., Munoz-Saez, C., Maksymowicz, A., & Ortega-Culaciati, F. (2019). Geometry of geyser plumbing inferred from ground deformation. *Journal of Geophysical Research: Solid Earth*, 124(1), 1072–1083. <https://doi.org/10.1029/2018jb016454>
- Aso, N., & Tsai, V. C. (2014a). Cooling magma model for deep volcanic long-period earthquakes. *Journal of Geophysical Research: Solid Earth*, 119, 8442–8456. <https://doi.org/10.1002/2014JB011180>
- Aso, N., & Tsai, V. C. (2014b). Cooling magma model for deep volcanic long-period earthquakes. *Journal of Geophysical Research: Solid Earth*, 119(11), 8442–8456. <https://doi.org/10.1002/2014jb011180>
- Banerdt, W. B., Smrekar, S. E., Banfield, D., Giardini, D., Golombek, M., Johnson, C. L., et al. (2020). *Initial results from the insight mission on mars*. *Nature Geoscience*. <https://doi.org/10.1038/s41561-020-0544-y>
- Bean, C. J., De Barros, L., Lokmer, I., Métaixian, J.-P., O’ Brien, G., & Murphy, S. (2014). Long-period seismicity in the shallow volcanic edifice formed from slow-rupture earthquakes. *Nature Geoscience*, 7(1), 71–75. <https://doi.org/10.1038/ngeo2027>
- Black, B. A., & Manga, M. (2016). The eruptibility of magmas at tharsis and syrtis major on mars. *Journal of Geophysical Research: Planets*, 121(6), 944–964. <https://doi.org/10.1002/2016je004998>
- Bramson, A. M., Byrne, S., Putzig, N. E., Sutton, S., Plaut, J. J., Brothers, T. C., & Holt, J. W. (2015). Widespread excess ice in arcadia planitia, mars. *Geophysical Research Letters*, 42(16), 6566–6574. <https://doi.org/10.1002/2015gl064844>
- Brown, J. R., & Roberts, G. P. (2019). Possible evidence for variation in magnitude for marsquakes from fallen boulder populations, Grjota Valles, Mars. *Journal of Geophysical Research: Planets*, 124, 801–822. <https://doi.org/10.1029/2018je005622>
- Brune, J. N. (1970). Tectonic stress and the spectra of seismic shear waves from earthquakes. *Journal of Geophysical Research*, 75(26), 4997–5009. <https://doi.org/10.1029/jb075i26p04997>

- Burr, D. M., Grier, J. A., McEwen, A. S., & Keszthelyi, L. P. (2002). Repeated aqueous flooding from the cerberus fossae: Evidence for very recently extant, deep groundwater on mars. *Icarus*, 159(1), 53–73. <https://doi.org/10.1006/icar.2002.6921>
- Burr, D. M., McEwen, A. S., & Sakimoto, S. E. H. (2002). Recent aqueous floods from the Cerberus Fossae, Mars. *Geophysical Research Letters*, 29. <https://doi.org/10.1029/2001GL013345>
- Cassanelli, J. P., & Head, J. W. (2018). Large-scale lava-ice interactions on mars: Investigating its role during Late Amazonian Central Elysium Planitia volcanism and the formation of Athabasca Valles. *Planetary and Space Science*, 158, 96–109. <https://doi.org/10.1016/j.pss.2018.04.024>
- Cattermole, P. (1987). Sequence, rheological properties, and effusion rates of volcanic flows at alba patera, mars. *Journal of Geophysical Research*, 92(B4), E553–E560. <https://doi.org/10.1029/jb092ib04p0e553>
- Ceylan, S., van Driel, M., Euchner, F., Khan, A., Clinton, J., Krischer, L., et al. (2017). From initial models of seismicity, structure and noise to synthetic seismograms for Mars. *Space Science Reviews*, 211(1–4), 595–610. <https://doi.org/10.1007/s11214-017-0380-6>
- Chouet, B. A. (1996). Long-period volcano seismicity: Its source and use in eruption forecasting. *Nature*, 380(6572), 309–316. <https://doi.org/10.1038/380309a0>
- Chouet, B. A., & Dawson, P. (2011). Shallow conduit system at kilauea volcano, hawaii, revealed by seismic signals associated with degassing bursts. *Journal of Geophysical Research*, 116(B12). <https://doi.org/10.1029/2011jb008677>
- Chouet, B. A., & Dawson, P. B. (2016). Origin of the pulse-like signature of shallow long-period volcano seismicity. *Journal of Geophysical Research: Solid Earth*, 121(8), 5931–5941. <https://doi.org/10.1002/2016jb013152>
- Chouet, B. A., & Matoza, R. S. (2013). A multi-decadal view of seismic methods for detecting precursors of magma movement and eruption. *Journal of Volcanology and Geothermal Research*, 252, 108–175. <https://doi.org/10.1016/j.jvolgeores.2012.11.013>
- Chouet, B. A., Page, R. A., Stephens, C. D., Lahr, J. C., & Power, J. A. (1994). Precursory swarms of long-period events at Redoubt Volcano (1989–1990), Alaska: Their origin and use as a forecasting tool. *Journal of Volcanology and Geothermal Research*, 62(1), 95–135. [https://doi.org/10.1016/0377-0273\(94\)90030-2](https://doi.org/10.1016/0377-0273(94)90030-2) (The 1989–1990 Eruptions of Redoubt Volcano, Alaska)
- Clifford, S., & Parker, T. J. (2001). The evolution of the martian hydrosphere: Implications for the fate of a primordial ocean and the current state of the northern plains. *Icarus*, 154(1), 40–79. <https://doi.org/10.1006/icar.2001.6671>
- Clinton, J. F., Giardini, D., Lognonné, P., Banerdt, B., van Driel, M., Drilleau, M., et al. (2017). Preparing for InSight: An invitation to participate in a blind test for Martian seismicity. *Seismological Research Letters*, 88(5), 1290–1302. <https://doi.org/10.1785/0220170094>
- Dawson, P. B., Chouet, B. A., & Power, J. (2011). Determining the seismic source mechanism and location for an explosive eruption with limited observational data: Augustine volcano, Alaska. *Geophysical Research Letters*, 38(3). <https://doi.org/10.1029/2010gl045977>
- Edwards, P. H., Bridges, J. C., Wiens, R., Anderson, R., Dyar, D., Fisk, M., et al. (2017). Basalt–trachybasalt Samples in Gale Crater, Mars. *Meteoritics & Planetary Science*, 52(11), pp. 2931–2410. <https://doi.org/10.1111/maps.12953>
- Ehlmann, B. L., Mustard, J. F., Murchie, S. L., Bibring, J.-P., Meunier, A., Fraeman, A. A., & Langevin, Y. (2011). Subsurface water and clay mineral formation during the early history of mars. *Nature*, 479(7371), 53–60. <https://doi.org/10.1038/nature10582>
- Ernst, R., Grosfils, E., & Mége, D. (2001). Giant dike swarms: Earth, venus, and mars. *Annual Review of Earth and Planetary Sciences*, 29(1), 489–534. <https://doi.org/10.1146/annurev.earth.29.1.489>
- Fehler, M. (1983). Observations of volcanic tremor at mount st. helens volcano. *Journal of Geophysical Research*, 88(B4), 3476–3484. <https://doi.org/10.1029/jb088ib04p03476>
- Feldman, W. C., Mellon, M. T., Gasnault, O., Maurice, S., & Prettyman, T. H. (2008). Volatiles on mars: Scientific results from the mars odyssey neutron spectrometer. In J. Bell (Ed.), *The martian surface: Composition, mineralogy and physical properties* (pp. 125–148). Cambridge University Press. <https://doi.org/10.1017/CBO9780511536076.007>
- Filiberto, J., & Treiman, A. H. (2009). The effect of chlorine on the liquidus of basalt: First results and implications for basalt genesis on mars and earth. *Chemical Geology*, 263(1), 60–68. <https://doi.org/10.1016/j.chemgeo.2008.08.025> (Halogens in Volcanic Systems and Their Environmental Impacts)
- Gallagher, K., Charvin, K., Nielsen, S., Sambridge, M., & Stephenson, J. (2009). Markov chain Monte Carlo (MCMC) sampling methods to determine optimal models, model resolution and model choice for Earth Science problems. *Marine and Petroleum Geology*, 26(4), 525–535. <https://doi.org/10.1016/j.marpetgeo.2009.01.003>
- Giardini, D., Lognonné, P., Banerdt, W. B., Pike, W. T., Christensen, U., Ceylan, S., et al. (2020). The seismicity of mars. *Nature Geoscience*. <https://doi.org/10.1038/s41561-020-0539-8>
- Giordano, D., Russell, J. K., & Dingwell, D. B. (2008a). Viscosity of magmatic liquids: A model. *Earth and Planetary Science Letters*, 271, 123–134. <https://doi.org/10.1016/j.epsl.2008.03.038>
- Giordano, D., Russell, J. K., & Dingwell, D. B. (2008b). Viscosity of magmatic liquids: A model. *Earth and Planetary Science Letters*, 271(1), 123–134. <https://doi.org/10.1016/j.epsl.2008.03.038>. Retrieved from <http://www.sciencedirect.com/science/article/pii/S0012821X08002240>
- Golombek, M., Kipp, D., Warner, N., Daubar, I. J., Ferguson, R., Kirk, R. L., et al. (2017). Selection of the insight landing site. *Space Science Reviews*, 211(1), 5–95. <https://doi.org/10.1007/s11214-016-0321-9>
- Golombek, M., Warner, N. H., Grant, J. A., Hauber, E., Ansan, V., Weitz, C. M., et al. (2020). Geology of the insight landing site on mars. *Nature Communications*, 11(1), 1014. <https://doi.org/10.1038/s41467-020-14679-1>
- Greeley, R., Foing, B. H., McSween, H. Y., Jr., Neukum, G., Pinet, P., van Kan, M., et al. (2005). Fluid lava flows in gusev crater, mars. *Journal of Geophysical Research*, 110(E5). <https://doi.org/10.1029/2005je002401>
- Grosfils, E. B., Aubele, J., Crumpler, L., Gregg, T. K. P., & Sakimoto, S. (2000). Volcanism on earth's seafloor and venus. In J. R. Zimbelman, & T. K. P. Gregg, (Eds.), *Environmental effects on volcanic eruptions: From deep oceans to deep space* (pp. 113–142). Boston, MA: Springer US. https://doi.org/10.1007/978-1-4615-4151-6_5
- Grott, M., Baratoux, D., Hauber, E., Sautter, V., Mustard, J., Gasnault, O., et al. (2013). Long-term evolution of the Martian crust-mantle system. *Space Science Reviews*, 174, 49–111. <https://doi.org/10.1007/s11214-012-9948-3>
- Grotzinger, J. P., Gupta, S., Malin, M. C., Rubin, D. M., Schieber, J., Siebach, K., et al. (2015). Deposition, exhumation, and paleoclimate of an ancient lake deposit, gale crater, mars. *Science*, 350(6257). <https://doi.org/10.1126/science.1257575>
- Harlow, D. H., Power, J., Laguerre, E., Ambubuyog, G., White, R. A., & Hoblitt, R. P. (1996). Precursory seismicity and forecasting of the june 15, 1991, eruption of mount pinatubo. In C. Newhall, & R. Punongbayan (Eds.), *Fire and mud, eruptions and lahars of mount pinatubo*, Philippines (p. 285–305). Univ. of Washington Press, Seattle.
- Hastings, W. K. (1970). Monte Carlo sampling methods using Markov chains and their applications. *Biometrika*, 57, 97–109. <https://doi.org/10.1093/biomet/57.1.97>
- Hauck, S. A., II, & Phillips, R. J. (2002). Thermal and crustal evolution of mars. *Journal of Geophysical Research*, 107(E7). <https://doi.org/10.1029/2001je001801> 6-1-6-19. Retrieved from <https://agupubs.onlinelibrary.wiley.com/doi/abs/10.1029/2001JE001801>

- Head, J. W., Wilson, L., & Mitchell, K. L. (2003). Generation of recent massive water floods at Cerberus Fossae, Mars by dike emplacement, cryospheric cracking, and confined aquifer groundwater release. *Geophysical Research Letters*, 30, 1577–1580. <https://doi.org/10.1029/2003GL017135>
- Horvath, D. G., Moitra, P., Hamilton, C. W., Craddock, R. A., & Andrews-Hanna, J. C. (2020). Evidence for geologically recent explosive volcanism in Elysium Planitia, Mars. *Earth and Planetary Astrophysics*. Retrieved from <https://arxiv.org/abs/2011.05956>
- Hotovec, A. J., Prejean, S. G., Vidale, J. E., & Gombert, J. (2013). Strongly gliding harmonic tremor during the 2009 eruption of redoubt volcano. *Journal of Volcanology and Geothermal Research*, 259, 89–99. <https://doi.org/10.1016/j.jvolgeores.2012.01.001> (The 2009 Eruption of Redoubt Volcano, Alaska)
- Hui, H., & Zhang, Y. (2007). Toward a general viscosity equation for natural anhydrous and hydrous silicate melts. *Geochimica et Cosmochimica Acta*, 71, 403–416. <https://doi.org/10.1016/j.gca.2006.09.003>
- InSight Mars SEIS Data Service. (2019). *SEIS raw data, Insight Mission. IGP, JPL, CNES, ETHZ, ICL, MPS, ISAE-Supaero, LPG, MFSC*. https://doi.org/10.18715/SEIS.INSIGHT.XB_2016
- InSight Marsquake Service. (2020). *Mars seismic catalog, InSight mission; V1 2/1/2020ETHZ, IGP, JPL, ICL, ISAE-Supaero. MPS, Univ Bristol. Dataset*. <https://doi.org/10.12686/a6>
- Jaeger, W. L., Keszthelyi, L. P., McEwen, A. S., Dundas, C. M., & Russell, P. S. (2007). Athabasca Valles, Mars: A lava-draped channel system. *Science*, 317, 1709–1711. <https://doi.org/10.1126/science.1143315>
- Jaeger, W. L., Keszthelyi, L. P., Skinner, J. A., Milazzo, M. P., McEwen, A. S., Titus, T. N., et al. (2010). Emplacement of the youngest flood lava on Mars: A short, turbulent story. *Icarus*, 205, 230–243. <https://doi.org/10.1016/j.icarus.2009.09.011>
- Julian, B. R. (1994). Volcanic tremor: Nonlinear excitation by fluid flow. *Journal of Geophysical Research*, 99(B6), 11859–11877. <https://doi.org/10.1029/93JB03129>
- Julian, B. R. (2000). Period doubling and other nonlinear phenomena in volcanic earthquakes and tremor. *Journal of Volcanology and Geothermal Research*, 101(1), 19–26. [https://doi.org/10.1016/S0377-0273\(00\)00165-7](https://doi.org/10.1016/S0377-0273(00)00165-7)
- Karlstrom, L., Hurwitz, S., Sohn, R., Vandemeulebrouck, J., Murphy, F., Rudolph, M. L., et al. (2013). Eruptions at lone star geyser, yellowstone national park, USA: 1. Energetics and eruption dynamics. *Journal of Geophysical Research: Solid Earth*, 118(8), 4048–4062. <https://doi.org/10.1002/jgrb.50251>
- Karlstrom, L., Murray, K. E., & Reiners, P. W. (2019). Bayesian markov-chain monte carlo inversion of low-temperature thermochronology around two 8 – 10 m wide columbia river flood basalt dikes. *Frontiers of Earth Science*, 7(90). <https://doi.org/10.3389/feart.2019.00090>
- Kawakatsu, H., Kaneshima, S., Matsubayashi, H., Ohminato, T., Sudo, Y., Tsutsui, T., et al. (2000). Aso94: Aso seismic observation with broadband instruments. *Journal of Volcanology and Geothermal Research*, 101(1), 129–154. [https://doi.org/10.1016/S0377-0273\(00\)00166-9](https://doi.org/10.1016/S0377-0273(00)00166-9)
- Kedar, S., Kanamori, H., & Sturtevant, B. (1998). Bubble collapse as the source of tremor at old faithful geyser. *Journal of Geophysical Research*, 103(B10), 24283–24299. <https://doi.org/10.1029/98jb01824>
- Keszthelyi, L. P., Denlinger, R. P., O'Connell, D. R. H., & Burr, D. M. (2007). Initial insights from 2.5d hydraulic modeling of floods in athabasca valles, mars. *Geophysical Research Letters*, 34(21). <https://doi.org/10.1029/2007gl031776>
- Keszthelyi, L. P., McEwen, A. S., & Thordarson, T. (2000). Terrestrial analogs and thermal models for martian flood lavas. *Journal of Geophysical Research*, 105(E6), 15027–15049. <https://doi.org/10.1029/1999je001191>
- Khan, A., & Connolly, J. A. D. (2008). Constraining the composition and thermal state of Mars from inversion of geophysical data. *Journal of Geophysical Research*, 113, E07003. <https://doi.org/10.1029/2007JE002996>
- Kiefer, W. S., & Li, Q. (2016). Water undersaturated mantle plume volcanism on present-day mars. *Meteoritics & Planetary Sciences*, 51(11), 1993–2010. <https://doi.org/10.1111/maps.12720>
- Kolzenburg, S., Di Genova, D., Giordano, D., Hess, K. U., & Dingwell, D. B. (2018). The effect of oxygen fugacity on the rheological evolution of crystallizing basaltic melts. *Earth and Planetary Science Letters*, 487, 21–32. <https://doi.org/10.1016/j.epsl.2018.01.023>
- Kumagai, H., & Chouet, B. A. (1999, 08). The complex frequencies of long-period seismic events as probes of fluid composition beneath volcanoes. *Geophysical Journal International*, 138(2), F7–F12. <https://doi.org/10.1046/j.1365-246x.1999.00911.x>
- Kumagai, H., Chouet, B. A., & Dawson, P. B. (2005, 04). Source process of a long-period event at Kilauea volcano, Hawaii. *Geophysical Journal International*, 161(1), 243–254. <https://doi.org/10.1111/j.1365-246x.2005.02502.x>
- Lesage, P., Mora, M. M., Alvarado, G. E., Pacheco, J., & Métxian, J.-P. (2006). Complex behavior and source model of the tremor at arenal volcano, costa rica. *Journal of Volcanology and Geothermal Research*, 157(1), 49–59. <https://doi.org/10.1016/j.jvolgeores.2006.03.047> (Arenal Volcano, Costa Rica)
- Liang, C., Crozier, J., Karlstrom, L., & Dunham, E. M. (2020). Magma oscillations in a conduit-reservoir system, application to Very Long Period (VLP) seismicity at basaltic volcanoes: 2. Data inversion and interpretation at Kilauea volcano. *Journal of Geophysical Research: Solid Earth*, 125(1), e2019JB017456. <https://doi.org/10.1029/2019JB017456>
- Lipman, P. W., & Banks, N. G. (1987). A'a flow dynamics, mauna loa 1984. In R. W. Decker, T. L. Wright, & P. H. Stauffer (Eds.), *Volcanism in Hawaii* (pp. 1527–1565). US Geol. Surv. Prof. Pap.
- Lipovsky, B. P., & Dunham, E. M. (2015). Vibrational modes of hydraulic fractures: Inference of fracture geometry from resonant frequencies and attenuation. *Journal of Geophysical Research: Solid Earth*, 120(2), 1080–1107. <https://doi.org/10.1002/2014jb011286>
- Lognonné, P., Banerdt, W. B., Giardini, D., Pike, W. T., Christensen, U., Laudet, P., et al. (2019). Seis: Insight's seismic experiment for internal structure of mars. *Space Science Reviews*, 215(1), 12. <https://doi.org/10.1007/s11214-018-0574-6>
- Lognonné, P., Banerdt, W. B., Pike, W. T., Giardini, D., Christensen, U., Garcia, R. F., et al. (2020). Constraints on the shallow elastic and anelastic structure of mars from insight seismic data. *Nature Geoscience*, 13(3), 213–220. <https://doi.org/10.1038/s41561-020-0536-y>
- Lyons, J. J., & Waite, G. P. (2011). Dynamics of explosive volcanism at fuego volcano imaged with very long period seismicity. *Journal of Geophysical Research*, 116(B9). <https://doi.org/10.1029/2011jb008521>
- Marra, W., Hauber, E., McLelland, S., Murphy, B., Parsons, D., Conway, S., et al. (2014). Pressurized groundwater outflow experiments and numerical modeling for outflow channels on Mars. *Journal of Geophysical Research: Planets*, 119. <https://doi.org/10.1002/2014je004701>
- Marsh, B. D. (1981). On the crystallinity, probability of occurrence, and rheology of lava and magma. *Contributions to Mineralogy and Petrology*, 78, 85–98. <https://doi.org/10.1007/BF00371146>
- Martire, L., Garcia, R. F., Rolland, L., Spiga, A., Lognonné, P. H., Banfield, D., et al. (2020). Martian infrasound: Numerical modeling and analysis of insight's data. *Journal of Geophysical Research: Planets*, 125(6), e2020JE006376. <https://doi.org/10.1029/2020JE006376>
- McNutt, S. R. (2005). Volcanic seismology. *Annual Review of Earth and Planetary Sciences*, 33(1), 461–491. <https://doi.org/10.1146/annurev.earth.33.092203.122459>
- Metropolis, N., Rosenbluth, A. W., Rosenbluth, M. N., Teller, A. H., & Teller, E. (1953). Equation of state calculations by fast computing machines. *The Journal of Chemical Physics*, 21, 1087–1092. <https://doi.org/10.1063/1.1699114>

- Munoz-Saez, C., Manga, M., Hurwitz, S., Rudolph, M. L., Namiki, A., & Wang, C.-Y. (2015). Dynamics within geyser conduits, and sensitivity to environmental perturbations: Insights from a periodic geyser in the el tatio geyser field, atacama desert, chile. *Journal of Volcanology and Geothermal Research*, 292, 41–55. <https://doi.org/10.1016/j.jvolgeores.2015.01.002>
- Nahm, A. L., Pendleton, M. W., & Kattenhorn, S. A. (2016). Cerberus fossae, mars: The case for dike intrusion-related formation and modification. *Acta Geologica Sinica – English Edition*, 90(s1), 173–174. <https://doi.org/10.1111/1755-6724.12957>
- Namiki, A., Rivalta, E., Woith, H., Willey, T., Parolai, S., & Walter, T. R. (2018, 12). Volcanic activities triggered or inhibited by resonance of volcanic edifices to large earthquakes. *Geology*, 47(1), 67–70. <https://doi.org/10.1130/g45323.1>
- Neal, C. A., Brantley, S. R., Antolik, L., Babb, J. L., Burgess, M., Calles, K., et al. (2019). The 2018 rift eruption and summit collapse of Kilauea volcano. *Science*, 363(6425), 367–374. <https://doi.org/10.1126/science.aav7046>
- Neuberg, J. W., Tuffen, H., Collier, L., Green, D., Powell, T., & Dingwell, D. (2006). The trigger mechanism of low-frequency earthquakes on montserrat. *Journal of Volcanology and Geothermal Research*, 153(1), 37–50. <https://doi.org/10.1016/j.jvolgeores.2005.08.008> (MULTIMO: Multi-Parameter Monitoring, Modelling and Forecasting of Volcanic Hazard)
- Nissen-Meyer, T., van Driel, M., Stähler, S. C., Hosseini, K., Hempel, S., Auer, L., et al. (2014). AxiSEM: Broadband 3-D seismic wavefields in axisymmetric media. *Solid Earth*, 5(1), 425–445. <https://doi.org/10.5194/se-5-425-2014>
- Ohminato, T., Chouet, B. A., Dawson, P., & Kedar, S. (1998). Waveform inversion of very long period impulsive signals associated with magmatic injection beneath kilauea volcano, hawaii. *Journal of Geophysical Research*, 103(B10), 23839–23862. <https://doi.org/10.1029/98jb01122>
- Panning, M. P., Pike, W. T., Lognonné, P., Banerdt, W. B., Murdoch, N., Banfield, D., et al. (2020). On-deck seismology: Lessons from InSight for future planetary seismology. *Journal of Geophysical Research*, 125(4), e2019JE006353. <https://doi.org/10.1029/2019JE006353>
- Parfitt, E. A., & Wilson, L. (2008). *Fundamentals of physical volcanology*. Malden, MA: Blackwell Pub.
- Pedersen, G. B. M., Höskuldsson, A., Dürig, T., Thordarson, T., Jónsdóttir, I., Riishuus, M. S., et al. (2017). Lava field evolution and emplacement dynamics of the 2014–2015 basaltic fissure eruption at Holuhraun, Iceland. *Journal of Volcanology and Geothermal Research*, 340, 155–169. <https://doi.org/10.1016/j.jvolgeores.2017.02.027>
- Petcovic, H. L., & Dufek, J. D. (2005). Modeling magma flow and cooling in dikes: Implications for emplacement of columbia river flood basalts. *Journal of Geophysical Research*, 110(B10). <https://doi.org/10.1029/2004jb003432>
- Pitt, A. M., & Hill, D. P. (1994). Long-period earthquakes in the long valley caldera region, eastern california. *Geophysical Research Letters*, 21(16), 1679–1682. <https://doi.org/10.1029/94gl01371>
- Plesa, A.-C., Padovan, S., Tosi, N., Breuer, D., Grott, M., Wicczorek, M. A., et al. (2018). The thermal state and interior structure of mars. *Geophysical Research Letters*, 45(22), 12198–12209. <https://doi.org/10.1029/2018gl080728>
- Power, J. A., Stihler, S. D., White, R. A., & Moran, S. C. (2004). Observations of deep long-period (DLP) seismic events beneath Aleutian arc volcanoes; 1989–2002. *Journal of Volcanology and Geothermal Research*, 138(3), 243–266. <https://doi.org/10.1016/j.jvolgeores.2004.07.005>
- Rivoldini, A., Van Hoolst, T., Verhoeven, O., Mocquet, A., & Dehant, V. (2011). Geodesy constraints on the interior structure and composition of mars. *Icarus*, 213(2), 451–472. <https://doi.org/10.1016/j.icarus.2011.03.024>
- Roberts, G. P., Matthews, B., Bristow, C., Guerrieri, L., & Vetterlein, J. (2012). Possible evidence of paleomarsquakes from fallen boulder populations, Cerberus Fossae, Mars. *Journal of Geophysical Research*, 117(E2). <https://doi.org/10.1029/2011je003816>
- Rogers, G., & Dragert, H. (2003). Episodic tremor and slip on the cascadia subduction zone: The chatter of silent slip. *Science*, 300(5627), 1942–1943. <https://doi.org/10.1126/science.1084783>
- Ruedas, T., & Breuer, D. (2017). On the relative importance of thermal and chemical buoyancy in regular and impact-induced melting in a mars-like planet. *Journal of Geophysical Research: Planets*, 122(7), 1554–1579. <https://doi.org/10.1002/2016je005221>
- Rust, A. C., Balmforth, N. J., & Mandre, S. (2008). The feasibility of generating low-frequency volcano seismicity by flow through a deformable channel. *Geological Society, London, Special Publications*, 307(1), 45–56. <https://doi.org/10.1144/SP307.4>
- Sambridge, M., & Mosegaard, K. (2002). Monte Carlo methods in geophysical inverse problems. *Reviews of Geophysics*, 40(3), 3–1–3–29. <https://doi.org/10.1029/2000RG000089>
- Schools, J. W., & Montési, L. G. J. (2018). The generation of barriers to melt ascent in the martian lithosphere. *Journal of Geophysical Research: Planets*, 123(1), 47–66. <https://doi.org/10.1002/2017je005396>
- Self, S., Thoradson, T., & Kesthelyi, L. (1997). Emplacement of Continental Flood Basalt Lava Flows (100, pp. 381–410). *Geophysical Monograph Series*.
- Self, S., Thordarson, T., Keszthelyi, L., Walker, G. P. L., Hon, K., Murphy, M. T., et al. (1996). A new model for the emplacement of columbia river basalts as large, inflated pahoehoe lava flow fields. *Geophysical Research Letters*, 23(19), 2689–2692. <https://doi.org/10.1029/96gl02450>
- Shaw, H. R. (1972). Viscosities of magmatic silicate liquids; an empirical method of prediction. *American Journal of Science*, 272, 870–893. <https://doi.org/10.2475/ajs.272.9.870>
- Shelly, D. R., Beroza, G. C., & Ide, S. (2007). Non-volcanic tremor and low-frequency earthquake swarms. *Nature*, 446(7133), 305–307. <https://doi.org/10.1038/nature05666>
- Squyres, S. W., Knoll, A. H., Arvidson, R. E., Clark, B. C., Grotzinger, J. P., Jolliffe, B. L., et al. (2006). Two years at meridiani planum: Results from the opportunity rover. *Science*, 313(5792), 1403–1407. <https://doi.org/10.1126/science.1130890>
- Tanaka, K. L. (1986). The stratigraphy of mars. *Journal of Geophysical Research*, 91(B13), E139–E158. <https://doi.org/10.1029/JB091iB13p0E139>
- Tao, C., Seyfried, W. E., Lowell, R. P., Liu, Y., Liang, J., Guo, Z., et al. (2020). Deep high-temperature hydrothermal circulation in a detachment faulting system on the ultra-slow spreading ridge. *Nature Communications*, 11(1), 1300. <https://doi.org/10.1038/s41467-020-15062-w>
- Taylor, J., Teanby, N. A., & Wookey, J. (2013). Estimates of seismic activity in the Cerberus Fossae region of Mars. *Journal of Geophysical Research: Planets*, 118(12), 2570–2581. <https://doi.org/10.1002/2013je004469>
- Thomas, A. M., Nadeau, R. M., & Bürgmann, R. (2009). Tremor-tide correlations and near-lithostatic pore pressure on the deep san andreas fault. *Nature*, 462(7276), 1048–1051. <https://doi.org/10.1038/nature08654>
- Thordarson, T., & Self, S. (1993). The Laki (Skaftár Fires) and Grímsvötn eruptions in 1783–1785. *Bulletin of Volcanology*, 55(4), 233–263. <https://doi.org/10.1007/bf00624353>
- Vandemeulebrouck, J., Roux, P., & Cros, E. (2013). The plumbing of old faithful geyser revealed by hydrothermal tremor. *Geophysical Research Letters*, 40(10), 1989–1993. <https://doi.org/10.1002/grl.50422>
- van Driel, M., Krischer, L., Stähler, S. C., Hosseini, K., & Nissen-Meyer, T. (2015). Instaseis: Instant global seismograms based on a broadband waveform database. *Solid Earth*, 6, 701–717. <https://doi.org/10.5194/se-6-701-2015>
- Vaucher, J., Baratoux, D., Toplis, M. J., Pinet, P., Mangold, N., & Kurita, K. (2009). The morphologies of volcanic landforms at central elysium planitia: Evidence for recent and fluid lavas on mars. *Icarus*, 200, 39–51. <https://doi.org/10.1016/j.icarus.2008.11.005>

- Vetere, F., Murri, M., Alvaro, M., Domeneghetti, M. C., Rossi, S., Pisello, A., et al. (2019). Viscosity of pyroxenite melt and its evolution during cooling. *Journal of Geophysical Research: Planets*, 124, 1451–1469. <https://doi.org/10.1029/2018JE005851>
- Vetterlein, J., & Roberts, G. P. (2009). Postdating of flow in Athabasca Valles by faulting of the Cerberus Fossae, Elysium Planitia, Mars. *Journal of Geophysical Research*, 114, E07003. <https://doi.org/10.1029/2009JE003356>
- Wadge, G. (1981). The variation of magma discharge during basaltic eruptions. *Journal of Volcanology and Geothermal Research*, 11(2), 139–168. [https://doi.org/10.1016/0377-0273\(81\)90020-2](https://doi.org/10.1016/0377-0273(81)90020-2)
- Wech, A. G., & Thelen, W. A. (2015). Linking magma transport structures at Kilauea volcano. *Geophysical Research Letters*, 42(17), 7090–7097. <https://doi.org/10.1002/2015gl064869>
- Wilson, L., & Head, J. W., III (1994). Mars: Review and analysis of volcanic eruption theory and relationships to observed landforms. *Reviews of Geophysics*, 32(3), 221–263. <https://doi.org/10.1029/94rg01113>
- Wu, S. M., Lin, F. C., Farrell, J., & Allam, A. (2019). Imaging the deep subsurface plumbing of old faithful geyser from low-frequency hydrothermal tremor migration. *Geophysical Research Letters*, 46(13), 7315–7322